COILING AND DEPLOYMENT MECHANICS OF TAPE-SPRINGS

H.H.N.D. Haggalla

208024T

Thesis submitted in partial fulfillment of the requirements for the degree Master of Science in Civil Engineering

Department of Civil Engineering

University of Moratuwa

Sri Lanka

December 2021

DECLARATION

I hereby witness that this thesis represents my original research work conducted after registration for the degree of MSc at Department of Civil Engineering, University of Moratuwa. It has not been submitted elsewhere or for any degree or diploma and the collaborative contributions and previous work related to current study have been stated and properly acknowledged.

Also, I hereby grant non-exclusive right to University of Moratuwa and its agents to archive and make accessible this dissertation, in whole or in part in print electronic or other medium. However, I (H.H.N.D. Haggalla) retain all the ownership to use this content in whole or part in publications (Article/ Book).

Signature: *UOM Verified Signature* Date: 15/12/2021

The above candidate has carried out research for the Masters under my supervision

Name of the supervisor: Dr. H.M.Y.C. Mallikarachchi

Signature of the supervisor: *UOM Verified Signature* Date: 15/12/2021

ABSTRACT

Recent advances in space exploration call for smaller space structures that can be reconfigured to achieve large surfaces when in operation. Compact, lightweight structures that can be folded or coiled up for launch have been made possible thanks to self-deployable booms. These can then be self-deployed in orbit to support a variety of small spacecraft systems. However, prior understanding of deployment behaviour is important before launch. This study focuses on model reduction techniques in predicting the deployment behaviour of coiled long-narrow thin shells known as tape springs. Coiling, stowage, and deployment stages that demonstrate considerable cross-section deformation of the tape-spring are discussed. The developed numerical benchmarking model well agrees with the theoretical framework that has previously been established in terms of deployment time and stored strain energy. This numerical model has further been used in a stage-wise development of a beam-shell hybrid model. The effect of varying hub radius is introduced to the existing theoretical framework to predict the coiling and deployment behaviour more accurately.

DEDICATION

"When twilight drops her curtain down - And pins it with a star

Remember that you have a friend - Though she may wander far."

— *L.M. Montgomery*

(1874-1942)

To my dearest friends,

Asitha, Kasun, Isuri, and Gayan,

Thank you.

I wouldn't have made it this far without you.

ACKNOWLEDGEMENT

My heartiest gratitude to Dr. H.M.Y.C. Mallikarachchi and Prof. W.P.S. Dias for the consistent supervision and resources that were given to me throughout this research and providing me the best exposure.

My heartiest thanks to Professor Simon Guest for the immense guidance and direction given to me on progressing through the research. Also, many thanks to all the other respective lecturers for assessing me during the research and for advising me on areas of improvement.

Special thanks to the Deployable structures research group for giving me motivation and guidance throughout the research.

Finally, I would like to convey my heartiest gratitude and respect to my dear parents who were always behind me giving me great strength and support and all my friends who have assisted me in many ways for the successful completion of this research.

H.H.N.D. Haggalla

Department of civil engineering

University of Moratuwa

TABLE OF CONTENTS

LIST OF FIGURES

LIST OF TABLES

LIST OF ABBREVIATIONS

STEM - Storable Tubular Extendible Member booms

CTM - Collapsible Tubular Masts

TRAC - Tubular Rollable, and Coilable booms

STACER - Spiral Tube and Actuator for Controlled Extension and Retraction

SIMPLE - Self-contained Linear Meter-class deployable

1D – One dimensional

2D – Two dimensional

MATLAB - MATrix LABoratory

MPC – Model Predictive Control

CAE – Complete Abaqus Environment

FE – Finite Element

FEM – Finite Element Method

BeCu - Beryllium Copper

S4R – 4 node general-purpose shell, reduced integration with hourglass control, finite membrane strains

B31 - 2 node linear generalized beam

1. INTRODUCTION

1.1 General

Deployable structures are prefabricated, transportable, and reusable structures that are used as alternative structures for temporary shelters, emergency shelters after natural disasters, temporary accommodation, accommodation at remote sites due to their speed and ease of erection. Deployable structures are particularly used in aerospace applications due to the limited availability of transportation space. Nowadays, NASA as well as other space organizations have begun to deploy small satellites in missions that were traditionally designated for larger satellites, in the hopes of reducing the cost of space systems and allowing for mass production. Small spacecrafts must nevertheless contain deployable antennas, radiators, solar panels, and other equipment to provide equal functionality to bigger satellites.

Compact, lightweight structures that can be folded or coiled up for launch have been made possible thanks to self-deployable booms. These can then be self-deployed in orbit to support a variety of small spacecraft systems. Engineers can use this additional boom performance to considerably increase the size of solar sails on small satellite platforms, perhaps improving propulsion performance. With the growing interests for small-scale, especially nano-scale satellites and space structures, two main constraints that have been identified are the stowed volume and the mass of the space structure. Hence, recent research has been focusing on structures that are storable yet deployable into large configurations in tackling such constraints (Mallol & Tibert, 2013).

As mentioned before, besides the common instruments that the satellite structure is required carry, one other main requisite is to place any scientific instruments away from the satellite to prevent any harm caused by electromagnetic effects from the satellite’s electronic hardware. Hence, there again, it is essential to have deployable systems to satisfy such requirements which will have to be tackled with limited power available in such space systems in space.

There are four main classes of booms namely Storable Tubular Extendible Member (STEM) booms, Collapsible Tubular Masts (CTM), BI-STEM booms and Tubular Rollable and Coilable (TRAC) booms (see Figure 1.1) (Mallol & Tibert, 2013). STACER (Spiral Tube and Actuator for Controlled Extension and Retraction by Surrey Satellite Technology Ltd) and SIMPLE (A Self-contained Linear Meter-class deployable by Air Force Research Laboratory) are also some more noteworthy examples of booms (Mallol & Tibert, 2013).

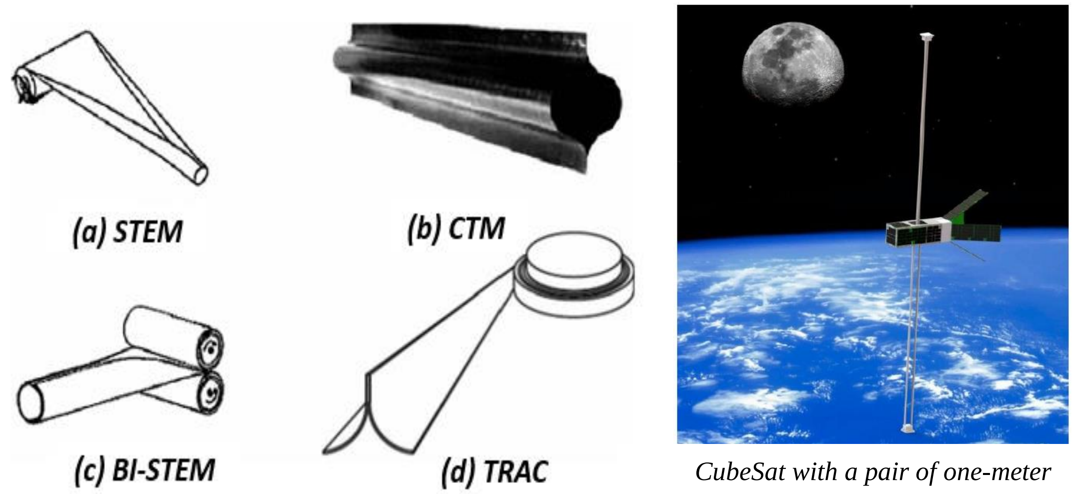

CubeSat with a pair of one-meter deployable ***SIMPLE*** *booms*

Figure 1.1: Main and subclasses of booms

The focus of this research is on booms that are considerably long, narrow, and manufactured as composite thin shell structures. Most of these complex boom systems cannot be deployed without the aid of motor mechanisms. In case the motor mechanism fails, then the deployment and other operations of the solar sail which takes place in space will fail. One solution would be to use strain-energy deployed booms which are also known as self-deployable booms. As the name suggests, the energy required for the deployment is provided by the strain energy stored during the packaging of the boom into a compact configuration (Wilson, 2017).

1.2 Cross-section deformations of booms

This study focuses on the coiling and deployment of an isotropic, linear-elastic, strain-energy deployed tape spring which is the most simplest form of booms and their results can be widely used in aerospace applications such as in elastic deployable structures. This can be predominantly treated as a thin shell problem. The geometrical configuration of a tape spring is as shown in Figure 1.2.

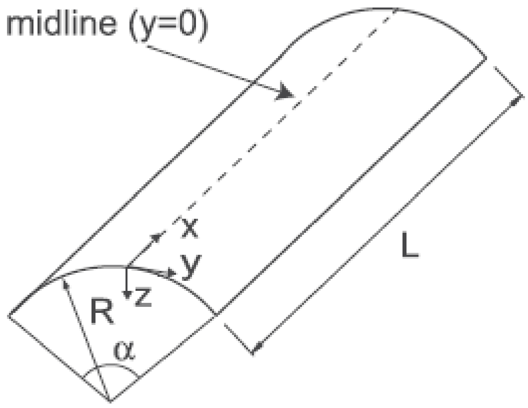

Figure 1.2: Geometry of tape springs

Slender elastic structures are prone to geometrical instabilities which result in loss of stiffness and severe deformations. Hence, it is of great importance to study their non-linear behaviour regarding the deployment of mechanical systems. These can be multiples of meters in length, but the cross-sections are of millimetre range hence, ramifications in attempting to develop computational models for such structures can be costly (Brinkmeyer et al., 2016), (Mallol & Tibert, 2013).

To capture the large deformations of coiling of a tape spring which predominantly behaves as a thin-walled beam, special cases of curved cross-sections must be addressed. They mainly involve three cases namely, (i) the flattened state, (ii) transition, and the (iii) undeformed state (see Figure 1.3).

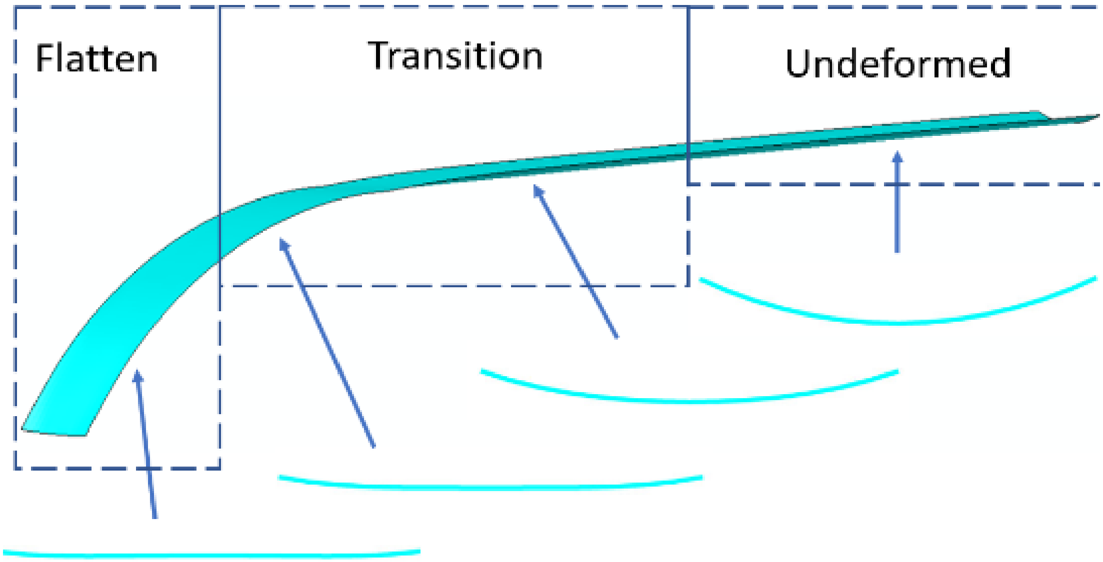

Figure 1.3: Three main regions of cross-section deformation of tape springs during coiling

1.3 Thesis background

The use of numerical analyses is vital in studying the mechanics of booms, and their designs from there onwards. In doing so, we must account for the cross-section deformations that occur during these coiling and deployment mechanisms which call for non-linear geometrical finite element analyses and these shell models comprise a very large number of degrees of freedom which ultimately make these numerical simulations expensive. Moreover, incorporation of contact conditions is critical due to the small packed configurations. Such conditions will have to be tackled using explicit analyses which may take minutes to hours or even days to complete running. There are various methods available to reduce the overall computational time of simulations but this may alter the results depending on the complexity of the problem. Some of the common techniques are the alteration of mesh size, use of mass scaling and rigid body constraints, use of symmetry etc. Beam-shell hybrid models are also such effective technique that can be explored in this sense where we can use low-order elements with a smaller number of degrees of freedom in regions with no significant cross-section deformation.

This can be approached mainly using 1D (beam element) or 2D (shell element). Utilizing only shell elements in the model will lead to a massive number of degrees of freedom to be handled which is advantages in achieving accurate results particularly at the locations with severe deformations but at the cost of high computational effort (Hoffait et al., 2010; Seffen et al., 2000; Soykasap, 2007). While in contrast, having a model only with low order elements such as beam elements will result in a simplified model which is more suitable in modelling the flattened and undeformed states (Gonçalves et al., 2010; Guinot et al., 2012; Pimenta & Campello, 2003; Živković et al., 2001). The transition region should be modelled with shell elements as it incorporates complex deformations hence, leading to a higher number of degrees of freedom (see Figure 1.4). Meanwhile, the stretching and bending energies involved due to stressing of flattened beam and shell's bending during the transition should be handled as well. Hence, discretization of the finite element model should be carried out to tackle the trade-off between computational effort and the order of elements to be used in capturing different states of deformation.

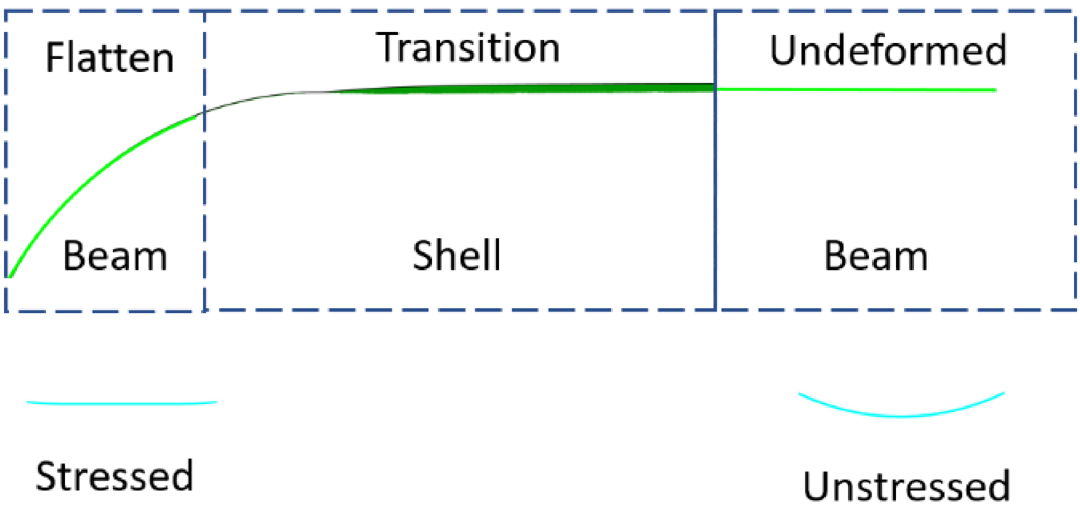

Figure 1.4: Idealized beam-shell hybrid model

1.4 Scope of the research

The present study focuses on the opposite sense coiling of a linear-elastic tape spring around a hub or a spool. For systems where these tape springs are in meters of lengths, given the complex geometrical and contact conditions, performing simulations for full shell models with such coiling behaviour can result in excessive hardware and software requirements and computational time. By thinking in advance about the basic engineering concepts that govern the structural behaviour we can take advantage of these concepts to simplify our numerical models without necessarily sacrificing the accuracy of the results. In this sense, initially a full shell model will be developed to capture the coiling and deployment behaviour of tape springs. After calibrating the full shell model with respect to parameters such as the curvature, stress distribution, deployment time and stored strain energy during coiling, an attempt will be made in producing a low order model (hybrid models with a combination of shell and beam elements) to capture the aforementioned coiling behaviour of tape springs with the aim of reducing the computational effort required. Essentially, the idea of the hybrid model would be to have beam elements in regions with less interest and use shell elements where severe deformation is expected. This way a finer mesh can be arranged for the regions with shell elements while achieving a faster simulation.

1.5 Aims and objectives

With the established scope in Section 1.4, the objectives of this research would be as follows;

- To develop a full shell model in capturing coiling and self-deployment of tape springs
- Using the full shell model as a benchmark, to develop a beam-shell hybrid model to reduce the computational cost associated with modelling of long narrow self-deployable structures

1.6 Methodology

As for the methodology, an extensive literature survey will be carried out focusing on the folding and coiling mechanics of linear elastic tape springs. This will supposedly result in a full shell model which will be used as a benchmarking model in validating the beam-shell hybrid model at the latter stages. An analytical study stated in Section 2 will be used in validating the benchmarking model in terms of deployment time and strain energy. As shown in Figure 1.5, once validated, the beam-shell hybrid model will be developed which will be further analysed to see any possible reductions of computational time with respect to the accuracy of results.

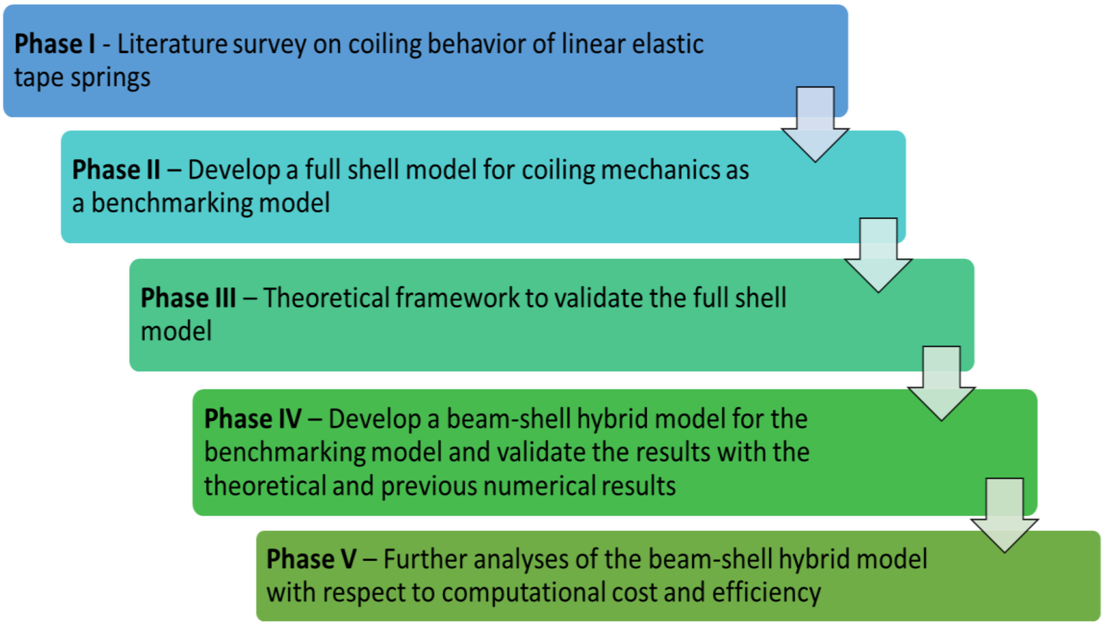

Figure 1.5: Flowchart for the proposed methodology

1.7 Outcomes and significance of the research

In terms of folding mechanics, extensive research has been carried out previously on the two main states of bending namely; equal and opposite bending whereas for coiling of tape springs, depending on the ratio between the spool radius to tape radius we get 3 main regions. They are the bending dominated region, tension dominated region and the region in between with loss of uniqueness. Tension dominated region is of importance because when the tape spring coils around the cylinder multiple times the effective hub radius would generally increase as a result of the tape thicknesses stacked on each other. Previous studies have seldom studied this in detail. Given the complex contact conditions and geometrical deformations involved in such behavior, use of numerical simulations in capturing this behavior has become vitally important. Due to the extensive computational time and resource requirements involved in this sense, developing low order hybrid models to reduce the aforementioned constraints is at the forefront of this research field which will also be attempted during the latter part of this study.

1.8 Arrangement of the thesis

The introduction, justification, and review of related works are included in **Chapters 1 and 2**. These two chapters recognized the most significant research gaps. The remainder of the thesis is broken down into three sections.

The benchmarking model is developed in **Chapter 3** using a detailed methodology**.** This was later used to develop the beam-shell hybrid models after validated against the theoretical results.

Chapter 4 includes an analysis of the results. Foremost, it presents the improvements made for the existing theoretical framework. Then the validation of the benchmarking model is presented. The stage-wise developments of the beam-shell hybrid model are presented in the latter part.

Chapter 5 delivers the conclusion of the research study and possible further extensions.

2. LITERATURE REVIEW

2.1 Introduction

2.1.1 Folding mechanics of tape springs

As far as folding of tape springs is considered, extensive research has been carried out previously focusing on the two main states of bending of tape springs; opposite (positive moment) and equal (negative moment) sense of bending as shown in Figure 2.1.

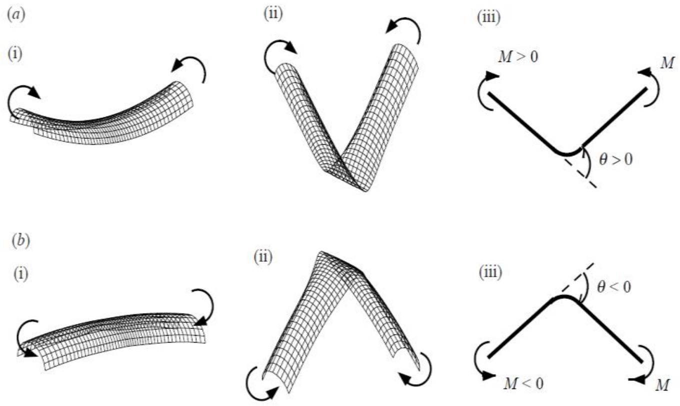

Figure 2.1: (a) Opposite and (b) equal sense bending

For small rotations, initially the moment *M* varies linearly with ϑ as the tape bends into a smooth curve. However, for larger rotations, the behavior of *M* depends on the sign of *M* as shown in the Figure 2.2.

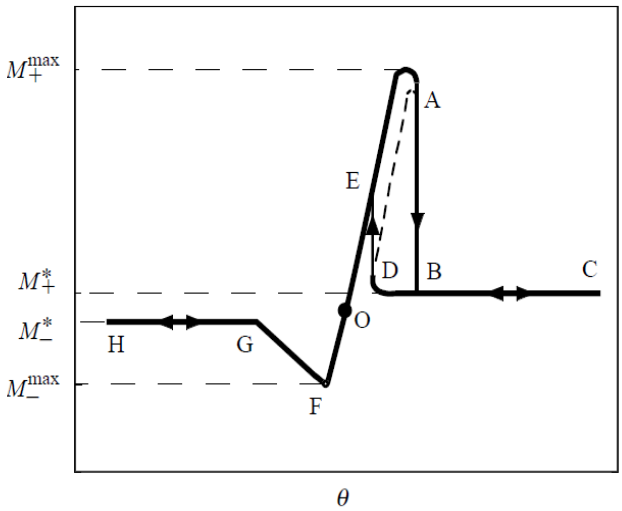

Figure 2.2: Moment-rotation relationship of folding of tape springs (Seffen, 1999)

During opposite sense bending the M will increase linearly while the tape spring cross-section flattens. This will lead to a sudden snap-through at the middle of the fold reducing the M drastically (jump from point A to B in Figure 2.2). As we further increase the rotation, M tends to remain constant (B to C) and it will follow the same path when the end moment is reversed (C to B). But when point B is reached it will not snap-back, rather it will reach point D and snap-through to point E resulting in a lower M and returns to the same loading path as the original.

During equal sense bending the linear behaviour between M and ϑ does not exist for a longer period due to the sudden bifurcation through point F to G in a flexural-torsional deformation mode. As the rotation is increased, the M tends to remain constant as earlier and when the M is reversed it returns to the same loading path as the original.

2.1.2 Coiling mechanics of tape springs

Predominantly, three regions have been identified concerning the coiling of tape springs (Wilson, 2017). These are categorized based on the tension force required during coiling for different coiling ratios which is the ratio between spool radius to tape spring radius (r_c/R) (see Figure 2.3).

- *Bending dominated* region → $r_c/R \leq 1$ → quadratic decrease of T as $r_c/R \to 1$
- *Transition* region → $1 < r_c/R < 3.424$ → $T \sim 0$
- *Tension dominated* region → $r_c/R > 3.424$ → linear increase of T with r_c/R

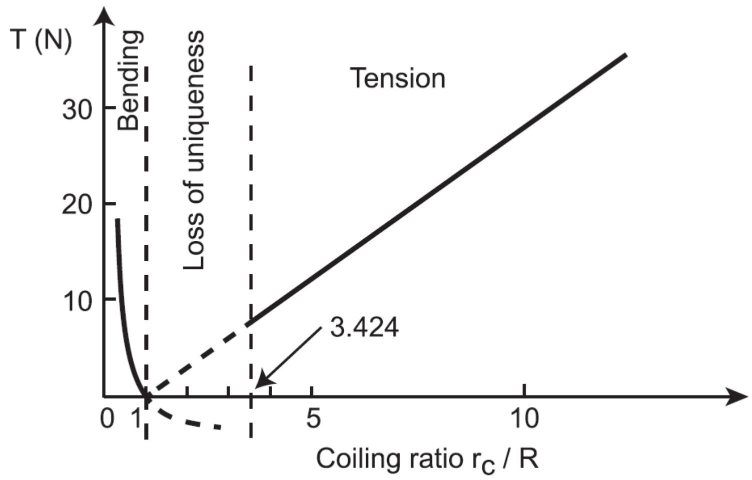

Figure 2.3: Three main regions in coiling of tape springs with respect to coiling ratio (Wilson, 2017)

Each region can be studied in detail as given in the sections below.

2.1.2.1 Bending-dominated region

In the bending dominated region, the relationship between '*T*' and '*r*' is formulated considering the bending strain energy of a fold with a general radius '*r*' and is bent a full circle by applying two equal and opposite axial forces '*T'* at the two tips of the tape spring as shown in Figure 2.4 (Wilson, 2017).

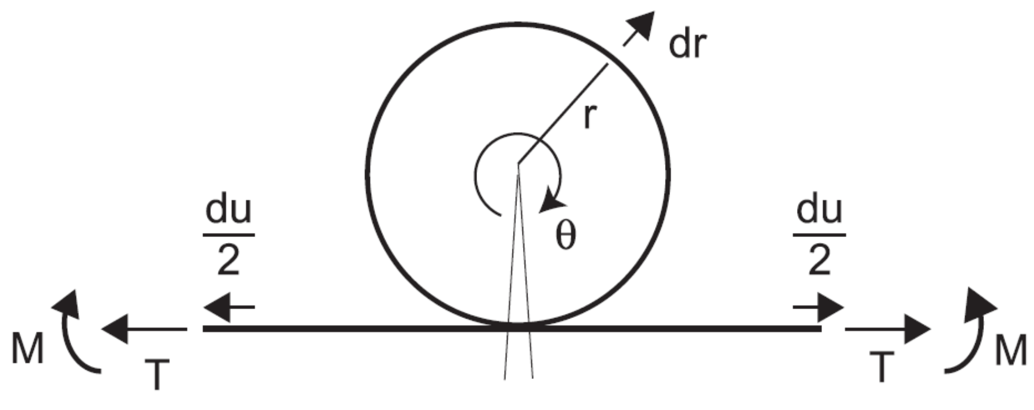

Figure 2.4: The curvature changes in a tape spring due to equal and opposite moments *M* applied. The (+) sign convention for *T, r, u* is shown (Wilson et al., 2020)

Consider the bending strain energy in the fold as given in Eq (2.1);

$$U(r) = \frac{D\alpha R\theta}{2}\left(\frac{r}{R^2} + \frac{2\nu}{R} + \frac{1}{r}\right) + U_{transition} \qquad (2.1)$$

Where D = $\frac{Eh^3}{12(1-\nu^2)}$

Consider a small movement of *du*/2 on either side of the end of tape spring due to a small change in *r* varying by *dr* while Θ is constant. Then we can write Eq (2.2) as follows.

$$\frac{dU}{dr} = \frac{D\alpha R\theta}{2}\left(\frac{1}{R^2} - \frac{1}{r^2}\right) \qquad (2.2)$$

The derivative of $U_{transition}$ is taken as zero as it is independent of r. Strain energy is due to the work done by the force 'T'.

$$dU = Tdu \tag{2.3}$$

But from geometry we know,

$$du = -\theta dr \tag{2.4}$$

By combining Eq. (2.2), (2.3) and (2.4) we get Eq.(2.5);

$$T = \frac{dU}{du} = \frac{dU}{dr}\frac{dr}{du} = \frac{D\alpha R}{2}\left(\frac{1}{R^2} - \frac{1}{r^2}\right) \tag{2.5}$$

Consider a cylinder with a radius r_c within the coiled spring. Then Eq.(2.5) can be rearranged and written as shown in Eq.(2.6);

$$T = \frac{D\alpha}{2R}\left(\left(\frac{R}{r_c}\right)^2 - 1\right) \tag{2.6}$$

The coiling behaviour studied in this region does not require any contact pressure between the hub and the tape spring. As shown in Figure 2.3, when r_c / R = 1 the tension force tends to become negative, i.e., a compressive force. Hence, the region where r_c / R >1 should be studied separately.

2.1.2.2 Loss of uniqueness region

As mentioned in Section 2.1.2, when forming a coil around a hub with a radius greater than the tape spring radius, i.e., when $r_c > R$, Eq. (2.6) suggests a compressive force to be applied which may lead to unstable configurations. One possible scenario is the development of a single or multiple localized folds with a radius of $R < r < r_c$ in short and long tape springs respectively. This has further been confirmed by the existence of lower energy modes in respective strain energies (Wilson, 2017).

By considering the geometries of single- and two-fold configurations, previous research has modified Eq.(2.6) to capture its strain energies. It has been found that beyond r_c / R >3.424, the two-fold configuration has the lowest strain energy. Hence, as far as a single fold is considered 3.424 is the limit coiling ratio r_c / R. The loss of uniqueness region will be considered for 1<r_c / R <3.424 and for r_c / R >3.424 will be considered under the tension-dominated region as discussed in Section 2.1.2.3 (Wilson, 2017).

2.1.2.3 Tension-dominated region

In the case where $r_c \ll R$, the tape spring will tend to expand during deployment. Localized folds will be formed when deploying a tape spring where $r_c \gg R$. A tension force can be applied at the tape spring or the gap between the casing and the tape spring can be restricted by the use of radial springs as shown in Figure 2.5.

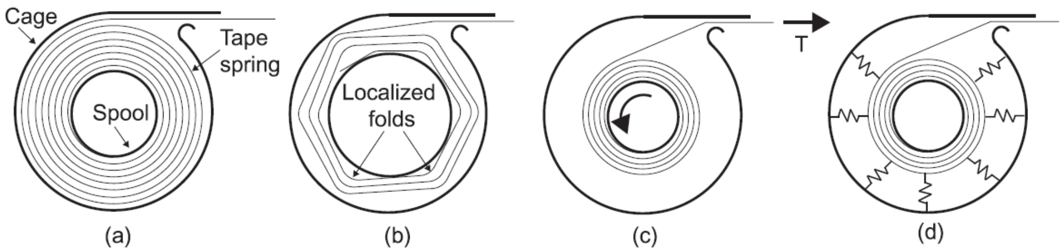

Figure 2.5: (a) A tape spring coiled around a spool (b) when partially uncoiled, creates localized folds stabilized by a (c) tension force or (d) radial springs (Wilson, 2017)

In particular, when r_c / R >3.424, coiling is obtained by the "transverse flattening of the tape spring by a fixed amount corresponding to the curvature change 1/R, followed by a decreasing amount of longitudinal bending of the flattened tape spring" (Wilson et al., 2020). However, when r_c / R >3.424 it is assumed that r_c>>>>>R hence, the longitudinal bending moment is assumed to be negligible. The coiling behavior is predominantly due to transverse pressure applied. But considering the equilibrium of the forces, the relationship between T and r_c / R can be derived.

As shown in Eq.(2.7), consider the equilibrium of the tape due to the tension force T and the transverse stress (derived using thin-shell theory) (see Figure 2.6).

$$2T = pDL \text{ ; where } D = 2r_c \tag{2.7}$$

Hence, we get T = pr$_c$; where p is the pressure per unit length

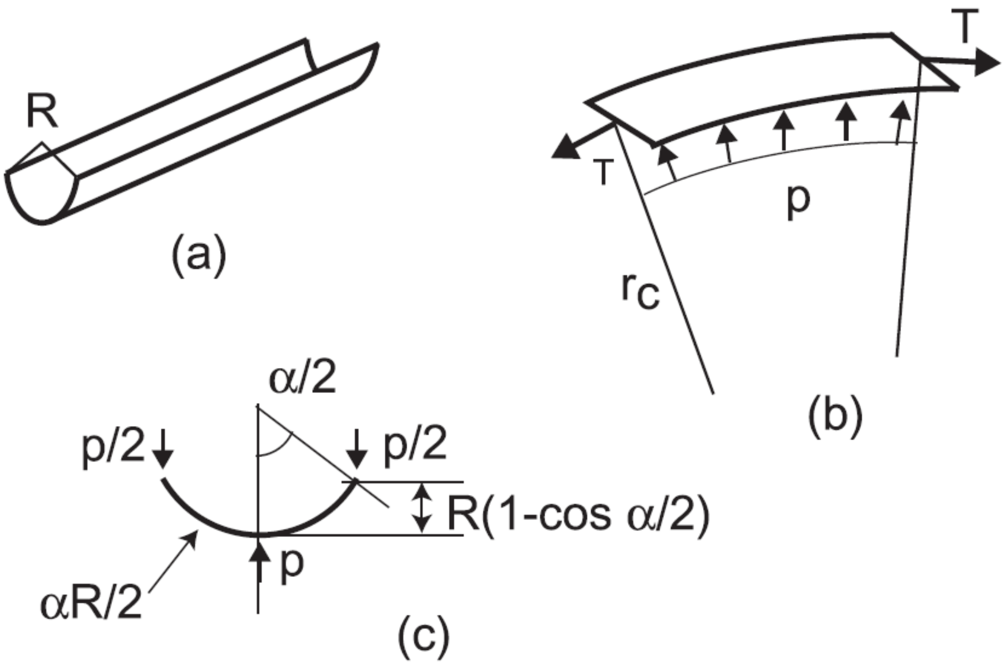

Figure 2.6: (a) Undeformed; (b) longitudinal bending and flattening; (c) transverse load application of the section (Wilson et al., 2020)

p can be derived using Eq.(2.8) by substituting a deflection of $\alpha R/2$ and a load of $p/2$ (Wilson et al., 2020):

$$\frac{\left(\frac{p}{2}\right)\left(\frac{\alpha R}{2}\right)^3}{3D} = R - R\cos\frac{\alpha}{2} \tag{2.8}$$

By substituting for p we get Eq.(2.9),

$$\mathrm{T} = \frac{48D\left(1-\cos\frac{\alpha}{2}\right)}{\alpha^3 R}\ \frac{r_c}{R} \tag{2.9}$$

As seen in the Eq.(2.9), in the tension-dominated region, T is linearly proportional to r_c / R. To develop a full shell benchmarking model for verification of results which can be later used to develop the beam-shell hybrid model, initially a case where $r_c \sim R$ will be considered as it will inherently form a coil with radius R with minimum complexities in its deployment behaviour. However, it is important to note that the third region mentioned above is what practically occurs where the effective spool radius will keep increasing during coiling due to the thickness of the tape spring. The effect of the tension force in this regard, especially when localized folds are being formed, has not been studied thoroughly.

2.1.3 Change in curvature in tape springs during coiling

The curvature change and the corresponding stress distribution of tape springs can be studied using a simple analytical model developed by Pedivellano & Pellegrino (2019) based on pure bending of a thin plate. In opposite sense coiling, when the tape spring is undeformed, the natural curvature vector can be written as shown in Eq. (2.10). Here x is in the longitudinal direction and y is in the transverse direction (see Figure 1.2).

$$K^0 = \begin{bmatrix} K_{xx}^0 \\ K_{YY}^0 \\ K_{xy}^0 \end{bmatrix} = \begin{bmatrix} 0 \\ \frac{-1}{r} \\ 0 \end{bmatrix} \tag{2.10}$$

The first order approximation for the curvature in opposite sense coiling can be derived as given in Eq.(2.11)

$$K^1 = \begin{bmatrix} K_{xx}^1 \\ K_{YY}^1 \\ K_{xy}^1 \end{bmatrix} = \begin{bmatrix} \frac{1}{R} \\ 0 \\ 0 \end{bmatrix} \tag{2.11}$$

This assumes a perfect flattening of the tape springs with no edge-effects. From this we can derive the curvature change that occurs during the coiling process as shown in Eq.(2.12a) and Eq.(2.12b).

$$\Delta K_x = K_x^1 - K_x^0 = -\frac{1}{R} \tag{2.12a}$$

$$\Delta K_y = K_y^1 - K_y^0 = \frac{1}{r} \tag{2.12b}$$

2.1.4 Stress distribution of tape springs during coiling

The strain distribution can be derived using the Kirchoff-Love plate theory (Pedivellano & Pellegrino, 2019) as shown in equations (2.13), (2.14) and (2.15). $\in_{xx}^0$, $\in_{yy}^0$ and $\in_{xy}^0$ corresponds to the mid-plane in plane strains. Ideally, for pure bending, these values should be zero.

$$\epsilon_{xx} = \epsilon_{xx}^{0} + \text{z}\ \Delta K_{xx} = \frac{-z}{R} \quad (2.13)$$

$$\epsilon_{yy} = \epsilon_{yy}^{0} + \text{z}\ \Delta K_{yy} = \frac{z}{r} \quad (2.14)$$

$$\epsilon_{xy} = \epsilon_{xy}^{0} + 2\ \text{z}\ \Delta K_{xy} = 0 \quad (2.15)$$

Using the constitutive model for an isotropic material, the stresses can be derived as shown in Eq.(2.16). With respect to the mid-surface of the shell, the stresses are expected to be symmetric.

$$\sigma = \frac{E}{1-\nu^2}\begin{bmatrix} 1 & \nu & 0 \\ \nu & 1 & 0 \\ 0 & 0 & \frac{1-\nu}{2} \end{bmatrix}\begin{bmatrix} \epsilon_{xx} \\ \epsilon_{yy} \\ \epsilon_{xy} \end{bmatrix} = \frac{E}{1-\nu^2}\begin{bmatrix} \frac{-z}{R} + \nu\frac{z}{R} \\ -\nu\frac{z}{R} + \frac{z}{R} \\ 0 \end{bmatrix} \quad (2.16)$$

Both the change in curvature and the predicted stress distribution from plate theory can be used in verifying the developed numerical model by comparing the curvature and the numerical stress in the model.

2.1.5 Experimental study of coiling with respect to tension force

With the aim of validating the theoretical results obtained in Section 2.1.2, an experiment pertaining to the tension-dominated region has been conducted pertaining to a coiling ratio $r_c/R = 4.3$ (Wilson, 2017). This result is further used as a reference in validating the numerical simulations performed with respect to the three main coiling regions (see Figure 2.3) as discussed in Sections 2.1.2.1, 2.1.2.2 and 2.1.2.3 (Wilson et al., 2020).

Essentially, a tape spring is coiled around a cylinder (paint can) (see Figure 2.7) and the force vs extension has been measured at different localized fold formations as expected in the tension-dominated region until the tape spring is fully enclosed with the cylinder radius (see Figure 2.8). It has been found that different coiling and uncoiling behaviors can be expected due to the instabilities exhibited in the force-extension behavior in the aforementioned experiment.

Figure 2.7: Experimental setup where the tape spring is enclosed around a cylinder (Wilson et al., 2020)

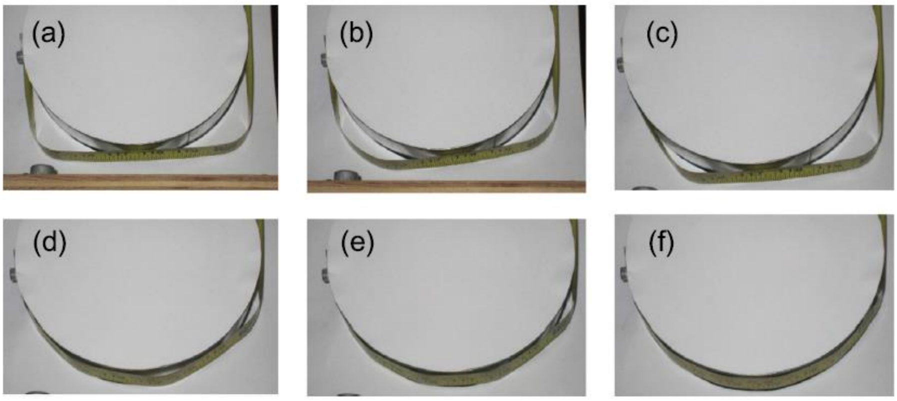

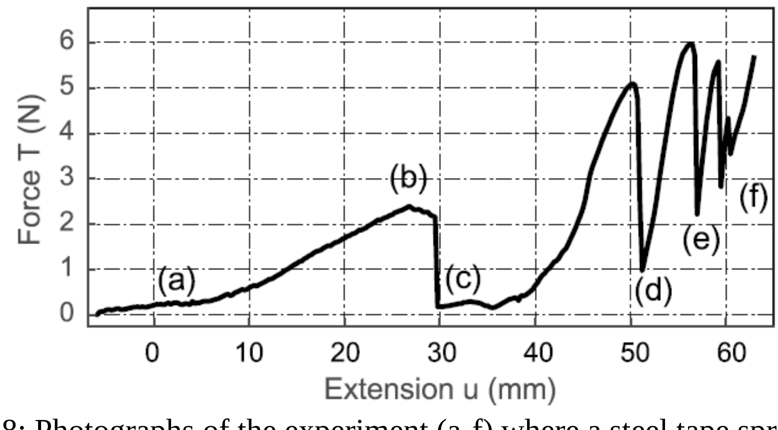

Figure 2.8: Photographs of the experiment (a-f) where a steel tape spring is enclosed around a steel cylinder and its corresponding averaged force profile vs. extension plot (over three repeated experiments) (Wilson et al., 2020)

Due to this, a series of numerical simulations have been performed with different radii scenarios in understanding the coiling and uncoiling of a tape spring on cylinders inclusive of the above reference experiment as well.

2.1.6 Numerical study of coiling with respect to tension force

This numerical technique has mainly focused on achieving a two-folded configuration forming a fully deployed configuration of a tape spring attached to a cylinder as shown in Figure 2.9.

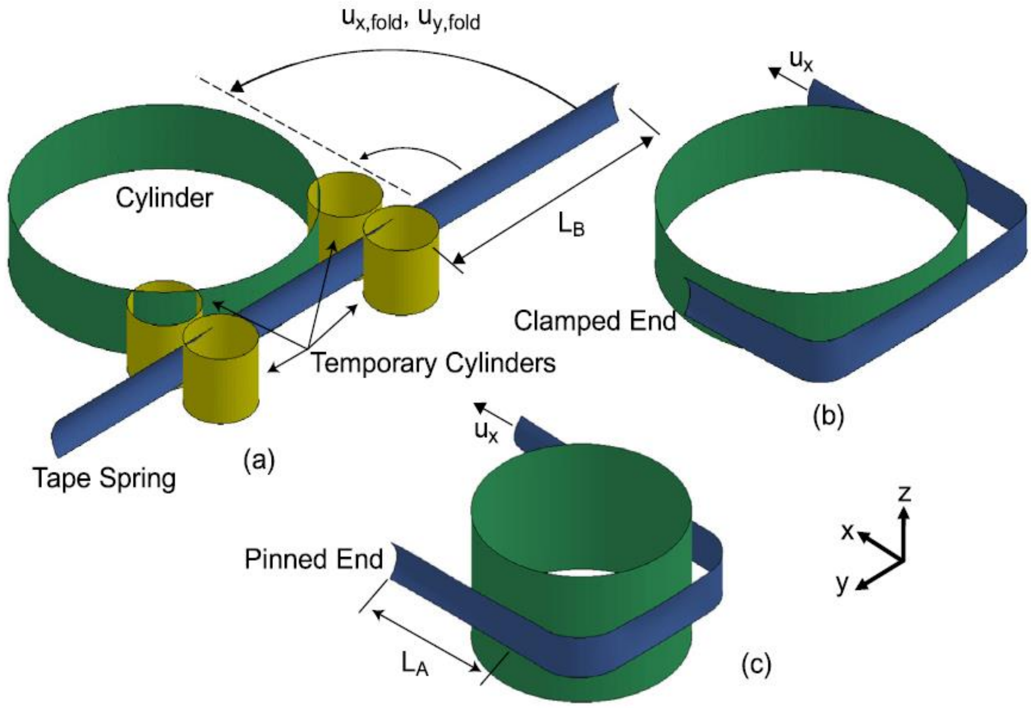

Figure 2.9: (a) By introducing the displacements $u_{x,fold}$, $u_{y,fold}$ two folds are created with the use of temporary cylinders which are later removed for cases (b) for $r_c / R > 3$ and (c) for $r_c / R < 3$. Later a displacement of u_x is applied (Wilson et al., 2020)

Two different boundary conditions; clamped and pinned (at a distance L_A = 100 mm, to avoid any unrealistic behaviour in the force), have been explored for tension-dominated region and bending-dominated region respectively when attaching the tape spring to the cylinder from one end. The fully coiled configuration was taken as the instance where the centreline of the tape spring conformed to the cylinder surface (see Figure 2.10) within three tape spring thicknesses when the coiling angle varies between 305^0 and 315^0. These ranges have been chosen to avoid any end effects near the clamped ends.

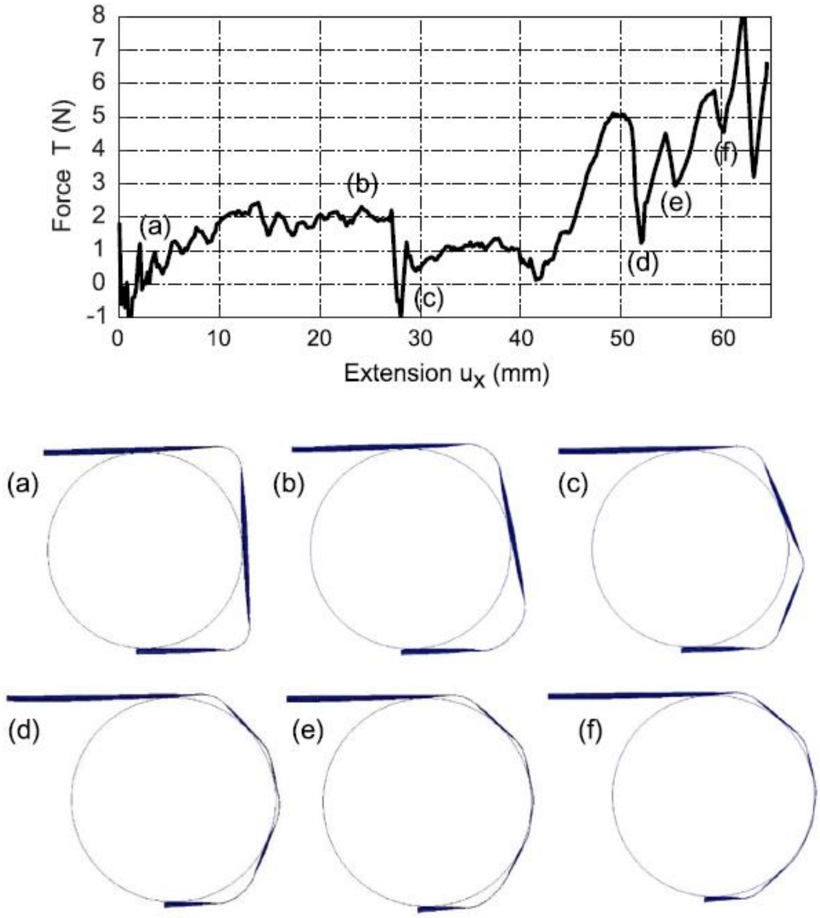

Figure 2.10: The graph of force against extension obtained from coiling simulation and its corresponding photographs of the simulation at points (a)–(f) (Wilson et al., 2020)

With coiling ratios varying between $0.4 < r_c / R < 5.25$, a series of numerical simulations have been performed adding up to a total of 20 cases with different coiling ratios and respective tension force required for fully coiling. All simulations have used the same tape spring properties (similar to the experiment, $\nu = 0.3$, $E = 210$ GPa, $\rho = 8050$ kg/m ^{3}, and $R = 19.2$ mm), and a cylinder radius ranging from 10 mm to 400 mm to study the tape spring behaviour corresponding to a range of coiling ratios (Wilson et al., 2020). As shown in Figure 2.11, it has been observed that the numerical results agree well with the theoretical results obtained in the graph shown in Figure 2.3.

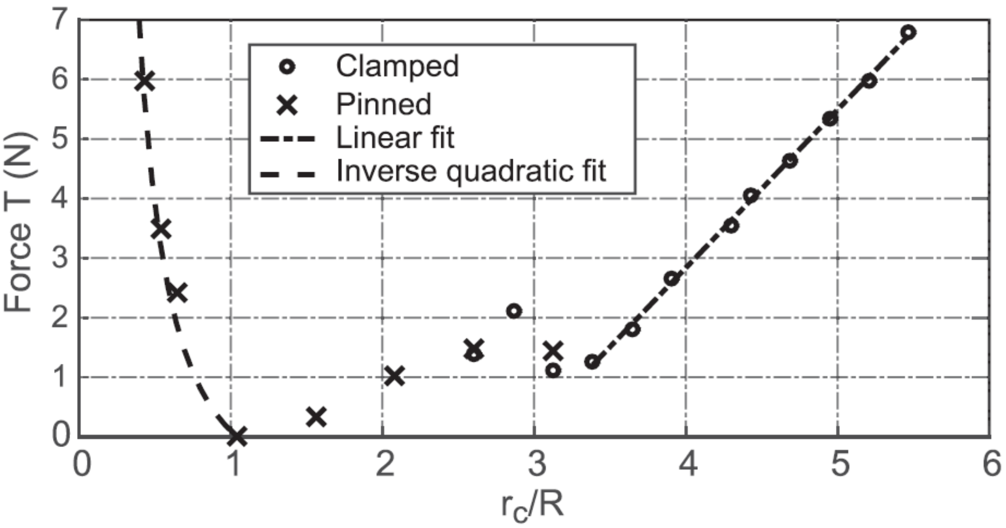

Figure 2.11: Experimental results for minimum tension force (to fully enclose the tape spring around the cylinder) vs. coiling ratio for different boundary conditions considered (clamped and pinned) (Wilson et al., 2020)

2.2 Theoretical framework for deployment ($\lambda_0=0$)

The equation of motion for the 2-dimensional deployment of a coiled spring where $r_c \sim R$ has been developed by the application of Lagrange's equations (Seffen, 1999) as shown in Eq.(2.17). As shown in Figure 2.12, two variable lengths have been defined in the tape spring; one being the straight part (L_{AB}) which supposedly remains tangent to the spool and the other being the coiled part around the spool (L_{BC}). λ is the ratio between the unspooled length to the total length of the tape spring whereas λ_0 is the ratio between the initial unspooled length to the total length of the tape spring. For a fully coiled state at the beginning of the deployment, this λ_0 value will be zero. ϑ is the subtended angle by the coiled part around the spool at any given time from which we can calculate the $L_{BC} = r\,\vartheta$.

$$\frac{1}{3}\rho(\mathrm{L}-r\vartheta)^3(\ddot{\zeta}+\ddot{\vartheta})+\frac{1}{2}\rho r(\mathrm{L}-r\vartheta)^2(\dot{\zeta}^2+\dot{\vartheta}^2)+\mathrm{D}\,(1\mp\nu)\alpha-\frac{1}{2}\rho r(\mathrm{L}-r\vartheta)^2\,\sin(\vartheta+\zeta)=Q_1 \quad (2.17)$$

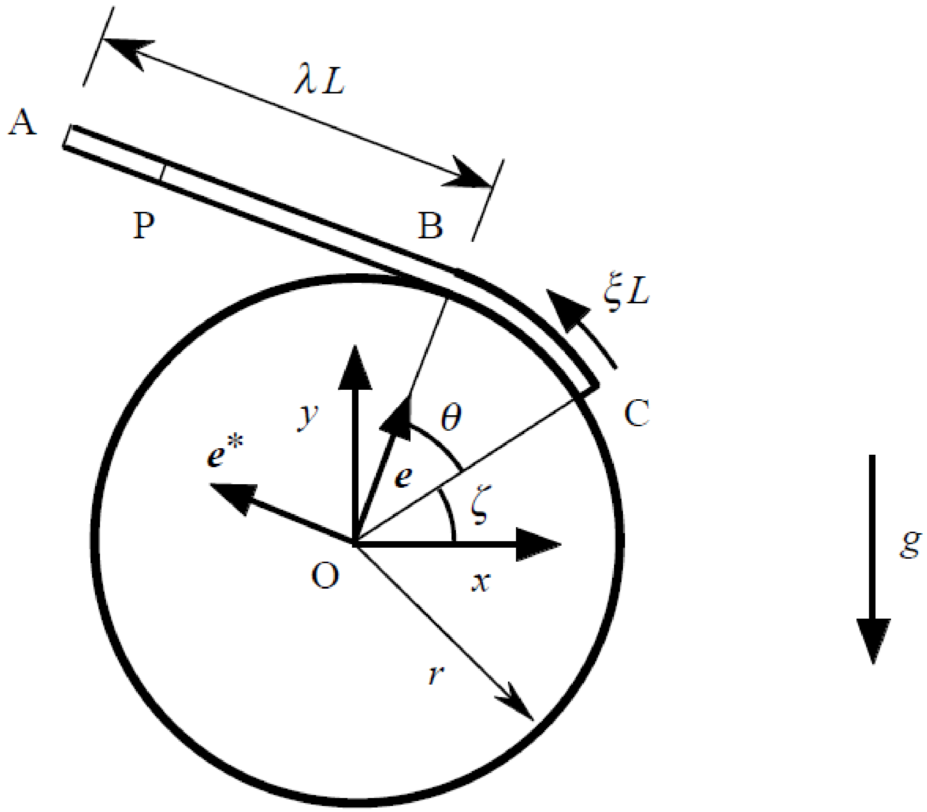

Figure 2.12: Configuration of a tape spring coiled around a hub that is free to rotate (Seffen, 1999)

A closed-form solution for the above said the result has been obtained for a case where a tape spring deploys in a gravity-free vacuum environment. By further working on this, the following ordinary differential equation has been obtained in terms of λ. Thus, substituting the drum rotation angle; angle between root of tape spring and horizontal ζ = 0, $\dot{\zeta}$ = 0 and $\ddot{\zeta}$ = 0, and setting g = 0 and Q_1 = 0, this simplifies to Eq.(2.18) and (2.19),

$$\frac{1}{3}\rho(L\text{-}r\vartheta)^3\ddot{\vartheta} - \frac{1}{2}\rho r(L\text{-}r\vartheta)^2\dot{\vartheta}^2 + \mu rR\alpha = 0 \tag{2.18}$$

$$\dot{\lambda} = \sqrt{\frac{6\mu r^2 R\alpha}{\rho L^4}}\;\frac{1}{\lambda} \tag{2.19}$$

By integrating Eq.(2.19), we get Eq.(2.20),

$$\lambda = \sqrt[4]{\frac{6\mu r^2 R\alpha}{\rho L^4}}\;\sqrt{2t} \tag{2.20}$$

Where λ is the ratio between the unspooled length to the total length of the tape spring, α is the angle subtended by the tape spring, R is the radius of the tape spring, r is the radius of the spool, L is the total length of the tape spring, μ is the strain energy density, ρ is the density of the tape spring material and t is the time. This resultant equation will be used as a reference in verifying the numerical results obtained from the benchmarking model. μ can be calculated using the following equations where ν is the poisons ratio, E is the material stiffness, and t is the tape spring thickness. For opposite sense bending strain energy per unit area, $\mu = \frac{D(1+\nu)}{R^2}$ and flexural rigidity $D = \frac{Eh^3}{12(1-\nu^2)}$

By rearranging the terms of Eq.(2.20) we get Eq.(2.21),

$$\lambda \, d\lambda = \sqrt{\frac{6\mu r^2 R\alpha}{\rho L^4}} \, dt \tag{2.21}$$

If we consider the integration of Eq.(2.21) as shown in Eq.(2.22) which can vary between 0 (fully coiled) to 1 (fully deployed), we can derive a value for T which is the total time taken for deployment. This provides an initial estimate for the total time that will be taken for full deployment which is given by Eq.(2.23).

$$\int_0^1 \lambda \;\; d\lambda = \sqrt{\frac{6\mu r^2 R\alpha}{\rho L^4}} \int_0^T dt \tag{2.22}$$

$$T = \frac{1}{2 * \sqrt{\frac{6\mu r^2 R\alpha}{\rho L^4}}} \tag{2.23}$$

2.3 Theoretical study (λ_0>0)

As derived in Eq.(2.24), when an unspooled length is present at the beginning of the deployment then, $\vartheta_0 = (1- \lambda_0)/r$ and $\vartheta = (1- \lambda)/r$ hence, by substituting these values for the aforementioned equation of motion for a gravity-free vacuum environment and simplifying further we get the following equation in terms of λ_0 and λ (Wilson, 2017).

$$\dot{\lambda} = \sqrt{\frac{6\mu r^2 R\alpha}{\rho L^4}} \sqrt{\frac{\lambda-\lambda_0}{\lambda^3}} \tag{2.24}$$

By integrating Eq.(2.24) concerning the time we get Eq.(2.25) which is quite useful in verifying the numerical results obtained from a benchmarking model where an unspooled length exists at the beginning of the deployment.

$$(\frac{\lambda}{2} + \frac{3\lambda_0}{4}) \sqrt{\lambda(\lambda - \lambda_0)} + \frac{3{\lambda_0}^2}{8} \ln \left| \left(\lambda - \frac{\lambda_0}{2}\right) + \sqrt{\lambda(\lambda - \lambda_0)} \right| - \frac{3{\lambda_0}^2}{8} \ln \left(\frac{\lambda_0}{2}\right) = \sqrt{\frac{6\mu r^2 R\alpha}{\rho L^4}}\ t \tag{2.25}$$

However, Eq.(2.25) can be complex to be solved manually hence, MATLAB solvers such as ode45, ode23, or ode113 can be recommended in solving this equation successfully. Wilson (2017) has used ode45.

2.4 Stored strain energy

During the coiling stage, the initial radius of coiling (r_{hub}) will keep on increasing to the final coiling radius (r) as shown in Eq.(2.26) due to the tape coiling multiple times around the hub until a particular final coiling angle (ϕ_{cf}) is reached given by Eq.(2.27).

$$r = r_{hub} + \frac{h_{tape}}{2} + 2h_{tape}\phi/2\Pi \tag{2.26}$$

$$\phi_{cf} = \frac{\Pi}{h_{tape}} \left[-\left(r_{hub} + \frac{h}{2}\right) + \sqrt{\left(r_{hub} + \frac{h}{2}\right)^2 + \frac{2L_{tape}h_{tape}}{\Pi}} \right] \tag{2.27}$$

Due to this reason, *r* can be defined as a function of the coiling angle from which the coiling angle for any given time can be calculated using Eq.(2.28) when the uncoiling angle is known.

$$\text{Coiling angle } \phi = \phi_{cf} - \Theta \tag{2.28}$$

According to (Mallol & Tibert, 2013), the strain energy (*U)* stored in a tape spring is released in the transition zone and the release rate per length (Q) is dependent on the coiling radius as defined in Eq.(2.29).

$$Q = \frac{U\,r}{L_{tape}} \tag{2.29}$$

Given the fact that r changes with time during uncoiling, the release rate of strain energy varies as well. Taking this into consideration, we can derive possible upper and lower bounds for the strain energy release rate per length and therefore for the deployment time of the tape spring which can be useful when analysing results.

2.5 Numerical modelling techniques

Although there have been many theoretical and especially a number of experimental studies on coiling behaviour, previous studies have seldom attempted to model the coiling behaviour of tape springs.

Mallol & Tibert (2013) have modelled the coiling sequence of a tape spring for a standalone boom as well as for a boom with a CubeSat model resulting in different end conditions at the boundaries (see Figure 2.13). Boundary conditions can affect the shock phases and post-deployment behaviour. This study had further identified the influence of varying hub radius on the deployment time as well as the rate of strain energy. It should be noted that the deployment time obtained from the numerical model is six times faster than the real prototype. The deployment time is extremely sensitive to contact conditions and material properties.

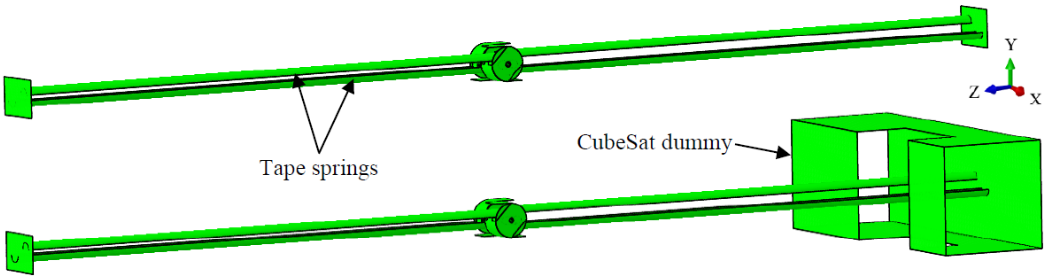

Figure 2.13: Standalone boom (fixed-free) and a boom with a CubeSat model (free-free) (Mallol & Tibert, 2013)

Wilson (2017) has conducted a series of experiments as well as numerical simulations for coiling of tape springs and has identified three main regimes of coiling behaviour depending on the tension force required for coiling with respect to each coiling ratio (see Figure 2.3). A central hub comprising of two cylinders and a spool around which the coiling and deployment of a tape spring has been considered (see Figure 2.14). The deployment time has been predicted by the numerical model by almost 100% accuracy with respect to previous experimental results obtained from a case study. This study has further identified the influence of initial unspooled length on the deployment time of tape springs.

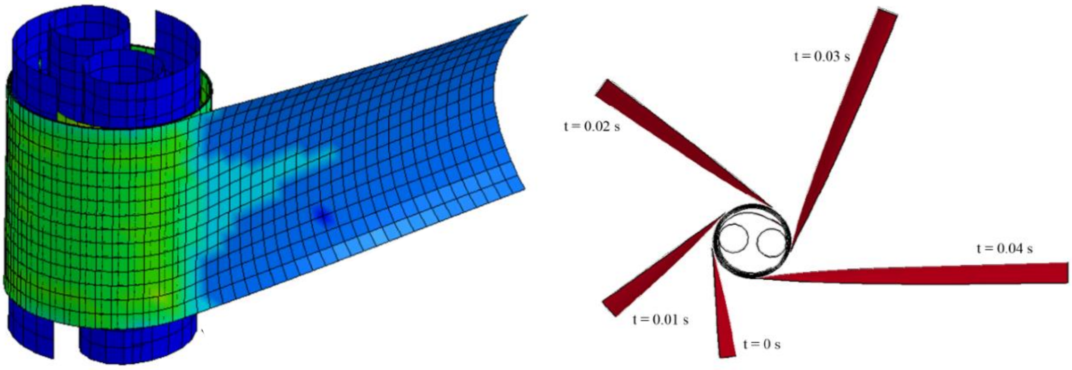

Figure 2.14: Coiled configuration and snapshots uncoiling of the tape spring using LS-Dyna (Wilson, 2017)

Pedivellano & Pellegrino (2019) have developed a "representative" numerical single coil that can represent the stowed coiled configuration of very long tape springs by assuming 'no-slip' condition and preservation of rotational symmetry. This representative coil can be analysed instead of the entire coiled system. Further they have performed stability analysis for this numerical developed model to obtain eigen values for different coiling ratios. It has been found that torsional modes are predominant in opposite sense coiling (see Figure 2.15) and this stability limit is quite low where as in equal sense coiling the first negative eigen value (stability limit) is a bending mode. It has also been found that the stability boundaries for opposite and equal sense coiling is unique for a given geometry and material regardless of the mode considered. However, accurate representation of the boundary conditions is crucial to capture the coiled behaviour. A single coil can be used effectively in capturing the stability behaviour of coiled tape springs irrespective of the number of coils in the actual problem considered.

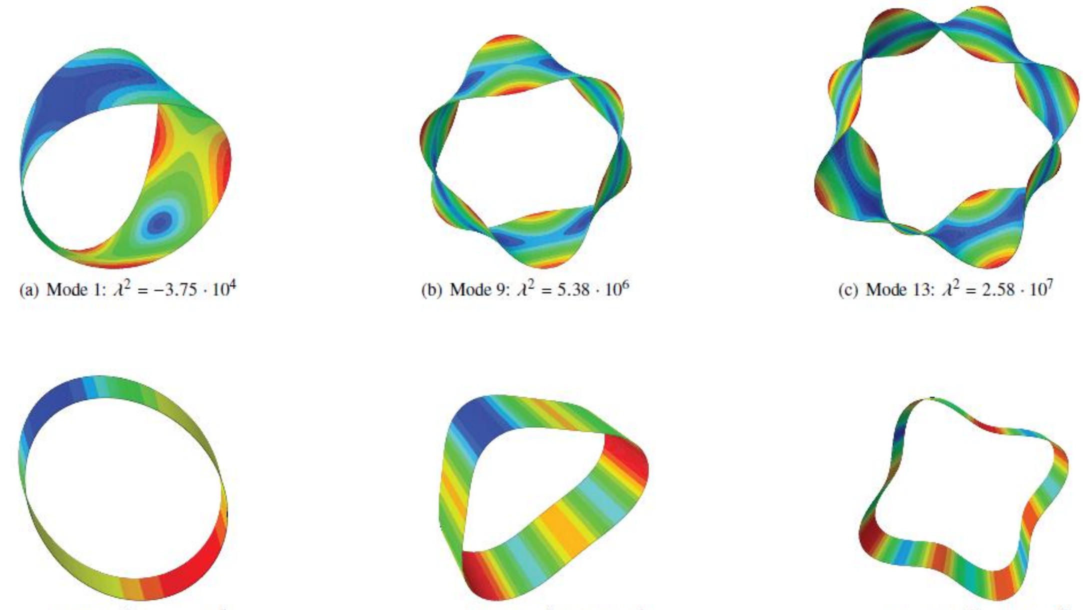

(a) Mode 1: $\lambda^2 = -3.75 \cdot 10^4$ (b) Mode 9: $\lambda^2 = 5.38 \cdot 10^6$ (c) Mode 13: $\lambda^2 = 2.58 \cdot 10^7$

(d) Mode 5: $\lambda^2 = 3.64 \cdot 10^5$ (e) Mode 8: $\lambda^2 = 4.76 \cdot 10^6$ (f) Mode 15: $\lambda^2 = 3.06 \cdot 10^7$

Figure 2.15: (a)-(c) torsional modes of opposite sense coil and (d)-(f) bending modes of equal sense coil obtained from the stability analysis

Numerous techniques are available that can be implemented in finite element modelling particularly to reduce the computational effort.

1. Use of symmetry
2. Co-simulation
3. Use of 1D and 2D elements (hybrid models)

The use of symmetry is one of the commonest techniques followed however, due to the complex deformation in the transition region in a coiled tape spring, it was decided not to consider symmetry neither in the longitudinal nor the transverse directions. Co-simulation is also an effective method for modelling components with complex contact conditions, large deformations, and/or dynamic responses, if used with the Explicit solver. In contrast, for components with small strains, Standard/ Implicit solvers can be used. But this comes with many limitations and challenges to be handled. Especially, the stability and accuracy of co-simulation region nodes that participate in a tie constraint, an MPC constraint, or a kinematic coupling constraint of the co-simulation solution may be adversely affected.

Numerical modelling of long, narrow deployable structures can be approached in 2 ways; one is to have full shell (2D) models which will lead to a massive number of degrees of freedom to be handled requiring sophisticated computer resources. This approach will produce results with high accuracy, however, at the cost of high computational effort. Hence, it is advantageous to limit this approach only to transition regions. In opposition to that, low order elements such as beam/rod elements will produce rather simplified models with few degrees of freedom hence, low computational effort. This approach is more advisable for modelling undeformed regions. Hence, for the transition region, a shell approach consisting of a full computation of a shell model in the framework of large displacements and large rotations can be adopted. Whereas for the flattened parts, using beam elements accounting for the transition of bending, simplified accurate models with very few degrees of freedom can be obtained. This type of beam-shell hybrid model will enable to reduce the computational time due to the reduced number of degrees of freedom in the considered problem while maintaining acceptable accuracy of the output results.

Sadowski (2019) has developed a beam-shell hybrid model for metal wind turbine support towers. These towers are very slender and tall in nature with a varying wall thickness usually greater in the lower regions when compared to the upper regions of the tower. The failure of these towers is usually localized and limited to the regions that exhibit plastic failure or buckling collapse and given the varying wall thickness of the tower, the failure regions can be predicted well in advance. Taking this into consideration, designers have the advantage of optimising the numerical model of the wind turbine support tower with respect to the type of finite elements used. For regions with higher interest shell elements can be incorporated and beam elements for the regions with less interest. The beam elements will not contribute to the failure mechanism. The saving from this mesh simplification will allow the designers to use finer mesh in shell regions that will lead to more accurate results while yielding faster solutions. MPC, kinematic coupling, tie constraints or sometimes even rigid body constraints has been used for the coupling between beam and shell interfaces using Abaqus/Standard as shown in Figure 2.16.

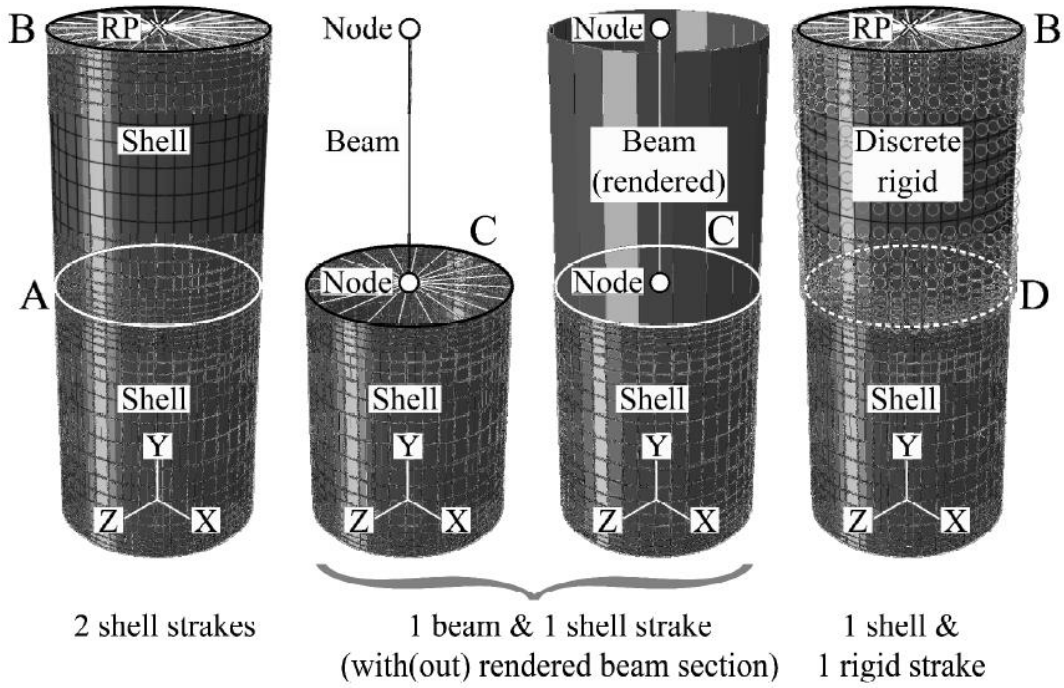

Figure 2.16: Coupling details between shell and beam regions in the hybrid model (Sadowski, 2019)

Similarly, a steel I-frame has been modelled using the hybrid modelling technique where shell elements have been used in the regions that are prone to elastic/inelastic local buckling and beam elements everywhere else (Sreenath et al., 2011). Although most steel designs are limited to linear elastic analyses and code-based limit state designs. Rigorous advances in research have been moving to modelling the inelasticity and second order effects incorporating material and geometrical nonlinearities as well. As mentioned in the wind turbine support tower, MPC and kinematic constraints have been considered in coupling the beam-shell interfaces however, only the translational degrees of freedom have been used when coupling to ensure in plane behaviour of the steel I-frame. Initially a full shell model has been developed and calibrated as per existing experimental results. This model has been used as a benchmark in developing the hybrid beam-shell model in the latter stages. The deformation profile and the stress distribution obtained for the full shell model as well as for the beam-shell hybrid model is shown in Figure 2.17 below.

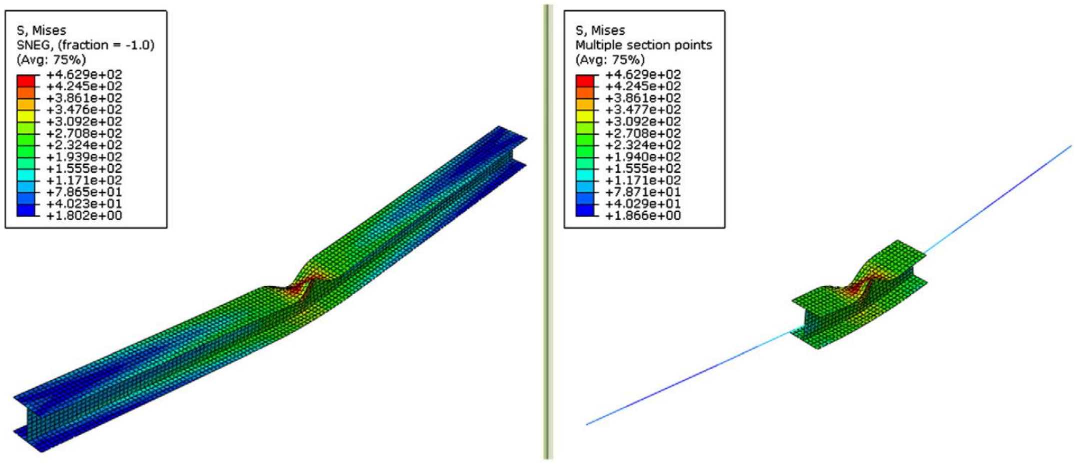

Figure 2.17: Stress distribution of full shell model (left) vs beam-shell hybrid model (right)

Evidently, it is of utmost importance to maintain a compatible number of active degrees of freedom at the beam-shell intersection to ensure proper bending moment and force transfer between the elements. MPC constraints, Kinematic coupling, Structural distributing coupling are a few techniques available in Abaqus in this sense. Few challenges need to be addressed when developing such hybrid models as certain criteria are problem-specific and should be known in advance. Namely,

1. Deciding the region for the shell elements in terms of its location and length, and

2. Bending moment and force transfer at the beam-shell interface

3. Import analyses as the beams get replaced by shells at different stages of the simulation

4. Bending moment and force transfer at the shell-shell interface

2.6 Summary of the chapter

This chapter highlights the key theoretical findings related to coiling and deployment mechanics of tape springs. Predominantly, 3 main regions have been established based on the relationship between the coiling ratio and the tension force (T) required. They are the bending-dominated region, tension-dominated region and the loss of uniqueness region in between. The bending dominated region exhibits a non-linear variation. In contrast, the tension-dominated region shows a linear variation. On the other hand, Seffen (1999) proposes a theoretical framework to capture the deployment time with respect to the ratio between initial unspooled length to the total length of the tape spring. This work has been further improved by Wilson (2017) to incorporate effects from initial unspooled lengths at the beginning of the deployment of the tape spring. Previous work has identified the importance of the variation of the hub radius during coiling which affects the strain energy release rate during deployment. This will be a point of interest in this study as well.

Moreover, numerical techniques considered for modelling coiling and deployment mechanics have also been discussed in this chapter. Several advantages and disadvantages have been considered relating to several techniques such as utilizing symmetry, co-simulation techniques and hybrid models comprising a combination of 1D and 2D elements. Ideally, the objective is to reduce the computational effort involved in simulating coiling and deployment mechanics of tape springs hence, the use of low-order (beam-shell hybrid) models will be emphasized in this study.

3. METHODOLOGY

Initially, a full shell model is developed which will be used as a benchmark to develop the beam-shell hybrid model in the next steps. In the benchmarking model, the tape spring will be flattened using a rigid roller and then coiled around a rigid hub/spool. Once fully coiled, it will be stowed in that coiled configuration for a few seconds before allowing it to dynamically deploy. The contact conditions used in the model are stated in the sections below. All material, geometrical and frictional coefficients were obtained from previous experimental studies.

The benchmarking model will be then calibrated with respect to following parameters.

1. Transverse and longitudinal curvature of the fold
2. Transverse and longitudinal stress distribution
3. Stored strain energy during coiling
4. Deployment time

Once calibrated and verified, an attempt will be made to develop a beam-shell hybrid model based on the benchmarking model. There the most critical regions will be modelled using shell elements where as the remaining will be modelled using beam elements. As the tape spring coils, regions with insignificant deformation will be replaced by beam elements while the previous stress conditions will be imported as predefined conditions to the new stages of the model using an import analysis. The beam-shell hybrid model will be developed in a series of steps as explained in the latter sections.

3.1 Benchmarking model and simulation conditions

As shown in Figure 3.1, the configuration of the numerical model considered consists of a tape spring which will be flattened and coiled using two rigid bodies: a roller at the top and a spool at the bottom.

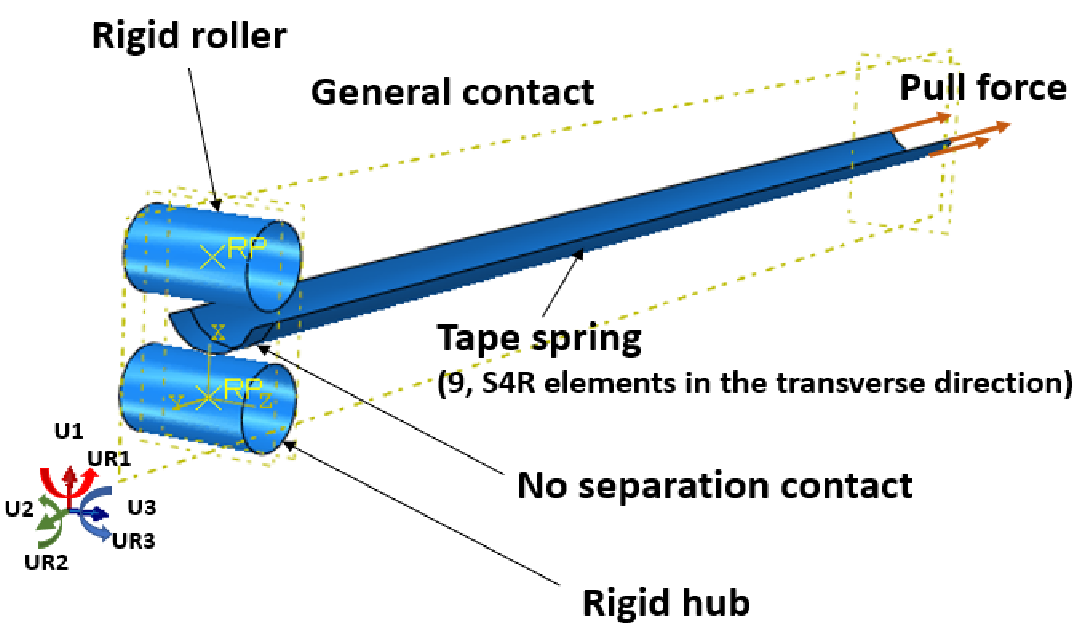

Figure 3.1: Numerical (benchmarking) model for coiling simulation

The material and geometrical parameters of the setup are tabulated as in Table 3.1 which are in par with annealed BeCu tape springs used in the bending experiments by Seffen (1999).

Table 3.1: Parameters used in the numerical model (Seffen, 1999)

The radius of tape spring (R)	0.0151 m
Radius of the hub (r_c)	0.0127 m
Length of tape spring (L)	0.5 m
Mass per unit length (ρ)	0.0293 kgm^{-1}
The angle of the embrace of cross-section (α)	2.3562
Young's modulus (E)	130 GPa
Poisson's ratio (v)	0.3
Strain energy per unit area (μ)	67.875 kgs^{-2}
Tape thickness (h)	0.0001 m
Flexural rigidity (D)	0.0119 kgm^{2}s^{-2}

The simulation is conducted using a commercially available structural analysis software ABAQUS/CAE 2017. Two Nos of Intel Core i9 7940X processors which provides computing performance for a desktop system by offering fourteen cores each were used to run the simulation. Three steps were defined namely, flattening (2.0 seconds), coiling (18.0 seconds), and deployment (8.0 seconds). Initially, a linear bifurcation analysis was performed for the tape spring, and was found that the fundamental period of the tape spring is 10.4 seconds. Hence, the coiling step was defined as 18.0 seconds to avoid any dynamic excitations in the model. Each boundary condition was applied with a smooth step amplitude definition. As shown in Figure 3.2, node regions were defined in the tape spring so that the boundary conditions can be conveniently activated as tabulated in the Table 3.2.

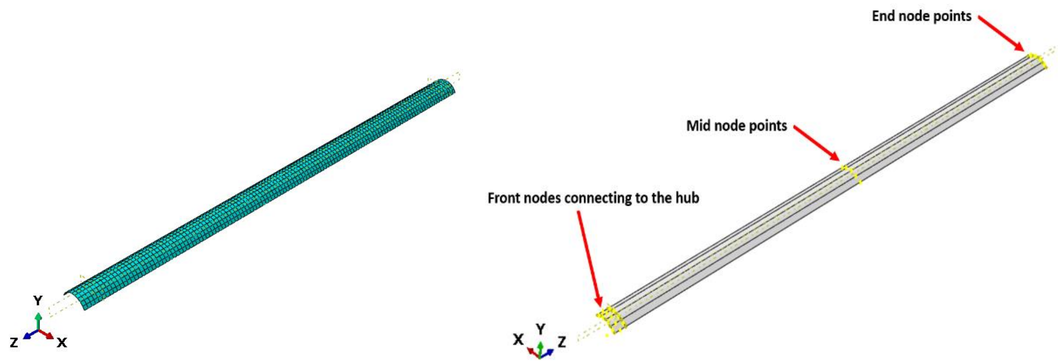

Figure 3.2: Mesh details and part geometry defined in the tape spring

Table 3.2: Loads and boundary conditions activated in the model

Description	Node set	Flattening 0-2 (s)	Coiling 2-20 (s)	Stowage 20-22 (s)	Deployment 22-22.5 (s)
Hub	Rigid bodies	UR3 = 36	UR3 = 36	UR3 = 0	UR3 = 0
Roller	Rigid bodies	U1 = -15	U3 = -100	U3 = -100	U3 = -100
Tape spring	End nodes	U3 = 0	U3 = 0	U3 = 0	Inactive
General contact applied (Frictionless)	All nodes	✓	✓	✓	✓

Surface to surface contact applied (Friction at the front end)	Front nodes	✓	✓	✓	✓
Apply a pulling/tension force at the free end of the tape spring	RP of roller		CF2 =-1N	CF2 = -N1	Inactive
Apply viscous pressure on the external faces of the tape spring	Surfaces of the tape spring		p = 5.2e^{-6}	p = 5.2e^{-6}	p = 5.2e^{-6}

A surface-to-surface friction contact is defined for the front-end node region that connects to the hub was used with a kinetic friction coefficient of 0.18 was used which was taken from experimental results from Wilson (2017) which suggests a kinetic friction coefficient of 0.18 $\pm$ 0.02. As in Figure 3.3, a strip of the tape spring is wrapped around a hub with one end being clamped to a loading beam of a material testing machine and the other being attached to a mass M. By obtaining an average force F (using a load cell) vs. the displacement by conducting the experiments for several times, this kinetic friction coefficient can be calculated using the Capston equation.

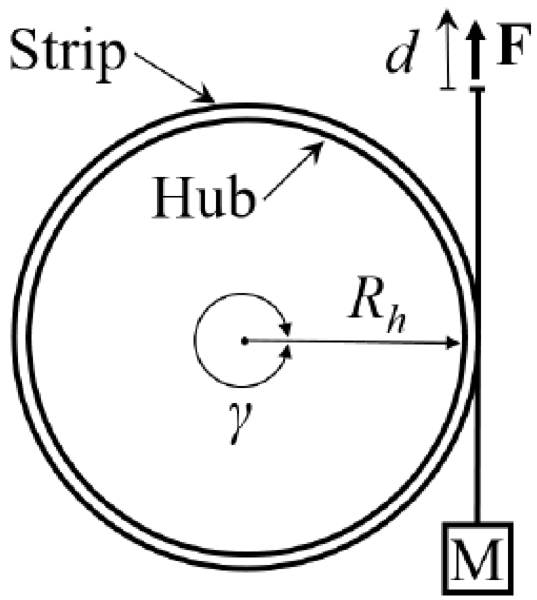

Capston equation:

$$T_{load} = T_{hold}\ e^{\mu\gamma}$$

$$\mu = \frac{\ln(\frac{T_{load}}{T_{hold}})}{\gamma}$$

Where,

T_{load} = F

T_{hold} = Mg

γ = 2π radians which is the total angle enclosed by the strip around the hub

Figure 3.3: Experimental setup to determine the kinetic friction coefficient between the surfaces of the tape spring and the hub

The penalty contact method is used as the mechanical constraint simulation as this is less restrictive when enforcing contact constraints between master and slave nodes. Moreover, it is more suitable for general type of contacts that involves contact between rigid bodies or when a single node has multiple contacts and especially when there are contact surfaces involving MPC constraints which are explored in the hybrid beam-shell model in the later sections.

Apart from the front edge of the tape which is attached to the hub using a surface-to-surface with a kinetic friction coefficient of 0.18, a frictionless general contact is defined for the surfaces everywhere else. The same penalty contact method is used as the mechanical constraint simulation here by default. When defining this contact condition, one should remember to exclude the surfaces that were already defined in the surface-to-surface contact, to avoid any contact issues.

A pull force of 1N was activated at the far edge of the tape spring. Given that the coiling ratio is $\frac{r_c}{R} = \frac{12.7}{15.1} = 0.84$ places this scenario within the bending-dominated region as shown in Figure 2.1. Hence, applying a pull force of approximately 1 N is quite acceptable.

S4 quadrilateral shell elements are useful for modelling thin components since only one element is needed through the thickness and also the thickness has no effect in the explicit solver calculations (Peterson & Mobrem, 2018). S4R elements; 4-node general-purpose shell, reduced integration with hourglass control, finite membrane strains are preferred due to their low computational cost. These are further preferred due to the avoidance of membrane and shear locking. However, some effects due to hourglassing cannot be avoided as full integration will not be executed. The minimum element edge length of the mesh was kept as 4mm ($\leq$ 1% of tape spring length=5mm) giving 9 elements in the transverse direction as shown by preliminary convergence studies for a sufficient level of accuracy (Seffen et.al, 2019) (see Figure 3.2).

An explicit solver is used as it is very robust and better able to capture the behaviour of quasi-static problems involving significant multiple contact conditions (Peterson &

Mobrem, 2018). This converges better and rarely aborts due to the failure of the numerical algorithm.

3.2 Challenges in simulating coiling behaviour

The flattening and coiling steps are simulated as quasi-static meaning that at any given time, we can assume the problem to be static. Hence, the loading should be applied slowly and smoothly as the rapid application of loading will lead to instabilities in the model. This can be achieved by using the Abaqus command **Amplitude, Definition* = *Smooth Step* (Mallikarachchi, 2011). A fifth-order polynomial transition between two amplitude values will be created such that the first and the second time derivatives are zero at the beginning and the end of the transition. On the other hand, this loading rate should be kept at a minimum while ensuring that dynamic excitations are not generated. The linear bifurcation analysis gives an idea as a starting point to decide this overall rate. As this is a quasi-static problem with significant contact conditions, an explicit solver is used.

The central difference operator used in explicit solver is conditionally stable. However, one should be cautious when working with the explicit solver as it requires comparatively smaller stable time increments to integrate over time to ensure stability in the simulation. The stable time increment should be limited because very small stability limits will lead to large number of increments so the simulation will take a longer time to complete. The stability limit can be approximated using Eq. (3.1) where C_d is the dilation wave speed as defined in Eq.(3.4) and L_{min} is the smallest element dimension in the mesh.

$$\Delta t \sim \frac{L_{min}}{C_d} \tag{3.1}$$

Evidently, the stable time increment is dependent on the mesh size, density and stiffness. Smaller mesh sizes and densities as well as larger stiffnesses will lead to smaller stable time increments, i.e., large number of increments hence, longer computational time. Moreover, in Abaqus/Explicit, the stable time increment is calculated per element hence, a single element with the smallest stable time increment can dominate and decide the simulation time of the entire model. To avoid such situations, the mesh verify tool in Abaqus can be used to identify such mesh elements/regions that will have stable time increments smaller than what is specified and alter their mesh sizes satisfactorily. In addition to that, the use of constraint such as MPC, tie, coupling or connectors in Abaqus/Explicit alone can lead to a longer computational time, especially with very fine mesh sizes. Hence, especially in the beam-shell hybrid models discussed in Section 4.4 and 4.6, it is crucial to strike a balance between the computational time and the stable time increment.

It is vitally important to check the energy balance to ensure that the simulation is producing a quasi-static response (Belytschko et al., 2000). Any instability will lead to artificial energy generation, hence, will violate the conservation of energy. The work applied by the external forces is almost equal to the internal energy of the model when a simulation is quasi-static. Hence, ideally, the total energy should be zero. Since the load is applied very slowly making the velocity small, the inertial forces will be negligible. This will result in almost zero kinetic energy. The thumb rule is that the kinetic energy should not be greater than 5% to 10% of internal energy if the simulation is to be quasi-static. Moreover, Abaqus provides the overall global energy of the system inclusive of the kinetic energy of any rigid bodies as well. Hence, when evaluating the energy balance, since the deformable bodies are only of interest, the kinetic energy of rigid bodies should be deducted from the total energy. The energy balance can be deduced by Eq.(3.2).

$$E_I + E_{KE} + E_{FD} + E_V + E_{IHE} - E_W - E_{PW} - E_{CW} - E_{MW} - E_{HF} = E_{total} \qquad (3.2)$$

where E_I is the internal energy, E_V is the viscous energy dissipated, E_{FD} is the frictional energy dissipated, E_{KE} is the kinetic energy, E_{IHE} is the internal heat energy, E_W is the work done by the externally applied loads, and E_{PW}, E_{CW}, and E_{MW} are the work done by contact penalties, constraint penalties, and propelling added mass, respectively. E_{HF} is the external heat energy through external fluxes.

Any excess kinetic energy in the system can be tackled either by defining appropriate varying loading rates, by applying numerical damping, or by mass scaling

(Mallikarachchi & Pellegrino, 2012). Since the inertial forces can be affected by mass scaling, that approach was not followed in this study. At this stage, numerical damping was also not studied. However, the loading rates were varied to avoid any excess kinetic energy in the model.

Vibration effects were observed in the tape spring at the end of the coiling stage. Hence, a viscous pressure load (p) of $2\text{x}10^{-4}\ \rho\ C_d$ was applied to damp out this dynamic effect enabling it to reach quasi-static equilibrium in a minimal number of increments. C_d is the dilation wave speed. In contrast to material damping that introduces damping in the interior of the body, this will absorb any pressure waves that will cross the free surface eliminating any energy reflected into the interior of the model. The viscous pressure is defined using Eq.(3.3).

$$p = -C_v\,(\bar{v}\,.\,\bar{n}) \tag{3.3}$$

p is the pressure applied to the body; C_v is the viscosity, given on the data line as the magnitude of the load; $\bar{v}$ is the velocity vector of the point on the surface where the viscous pressure is being applied; and $\bar{n}$ is the unit outward normal vector to the surface at the same point. Generally, it is recommended to use 1 or 2% of ρC_d where ρC_d is defined by Eq.(3.4). Here, ρ is the density of the material whereas E and ν are as given in Table 3.1.

$$\rho\,C_d = \rho\sqrt{\frac{E(1-\nu)}{\rho(1-\nu)(1+2\nu)}} \tag{3.4}$$

For the simulation to remain quasi-static, the kinetic energy and the viscous dissipation energy should be a very low fraction of the internal energy in the model.

3.3 Ploy region

In Section 2.5, the importance of knowing the location and length of the shell element region has been highlighted. Because the utilisation of shell elements predominates the computational efficiency of the model. In the context of coiling of tape springs, the ploy region, i.e., the transition region between the flattened and undeformed regions is critical as it is responsible for maintaining the strain energy gradient during coiling.

Moreover, whatever the strain energy stored during coiling will be released through this ploy region allowing the tape spring to self-deploy. In comparison to ploy regions in uniform bending where the strain energy in the folded tape spring is assumed only to be due to the fold alone (Calladine, 1998), the ploy region in coiling holds significant influence on its behaviour hence, can be deemed to be modelled using shell elements.

This raises concerns for the accurate estimation of the ploy region length. Previous work has focused on calculating the ploy length in bending of orthotropic tape springs as presented in Eq.(3.5) (Seffen et al., 2019).

$$L_p = \frac{1}{\sqrt{70}} \cdot \frac{1}{\beta^{\frac{1}{4}}} \cdot \frac{b^2}{R^{\frac{1}{2}} t^{\frac{1}{2}}} \tag{3.5}$$

Where L_p is the ploy length, b is the arc-width, R is the tape spring radius and t is the tape thickness and β is the orthotropic modular ratio. Given that β =1 for isotropic tape springs, an attempt was made to check the applicability of this equation with respect to ploy regions in coiling. However, it has been mentioned that the use of projected width for b instead of arc-width or rather, the best combinations of parameters to be used should be confirmed with more data and this is still part of on-going research. As shown in Figure 3.4, the ploy length obtained from the numerical model was compared against the theoretical ploy length calculated using Eq.(3.5) when b is equal to the arc width and the projected arc width respectively. It was observed that in the benchmarking model, ploy length is most compatible when the projected arc length is used in the equation. Confirmation on these needs more studies however, this gives an initial estimation for the length of the ploy region that needs to be modeled using shell elements in the hybrid model.

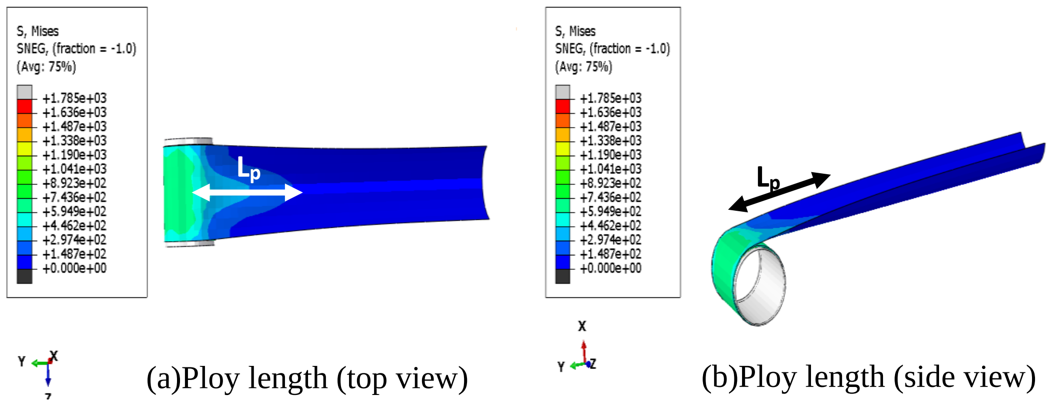

(a)Ploy length (top view) (b)Ploy length (side view)

Figure 3.4: Top and side configurations of ploy region

3.3.1 Locations and lengths of shell elements

Considering the results obtained in Section 3.3, it is evident that the ploy region should be modelled using shell elements. In addition to that, the flattened region which has the maximum stress and stored strain energy should be modelled using shell elements as well as it would be required in deployment simulation. As far as coiling is considered, attempts can be made to use beam elements instead of shell elements for the flattened region however, it is not considered in this study. As for the undeformed regions, beam elements can be used. As discussed in Section 3.6 later, a length equal to whatever the length coiled in the 1st stage of the simulation should be overlapped in the 2nd stage hence, the total length of the shell element region can be estimated to be the addition of the ploy length and twice the coiled length. However, as mentioned earlier, this statement has to be studied further in detail and validated before using in extensive research studies.

3.4 Beam-Shell hybrid model – Stage 01

The validated model is modified into a hybrid model as shown in Figure 3.5 by modelling a 160 mm length of the tape using S4R, 4-node general-purpose shell, reduced integration with hourglass control, finite membrane strains whereas the remaining length of 340 mm is modelled using B31, 2 node linear generalized beam sections.

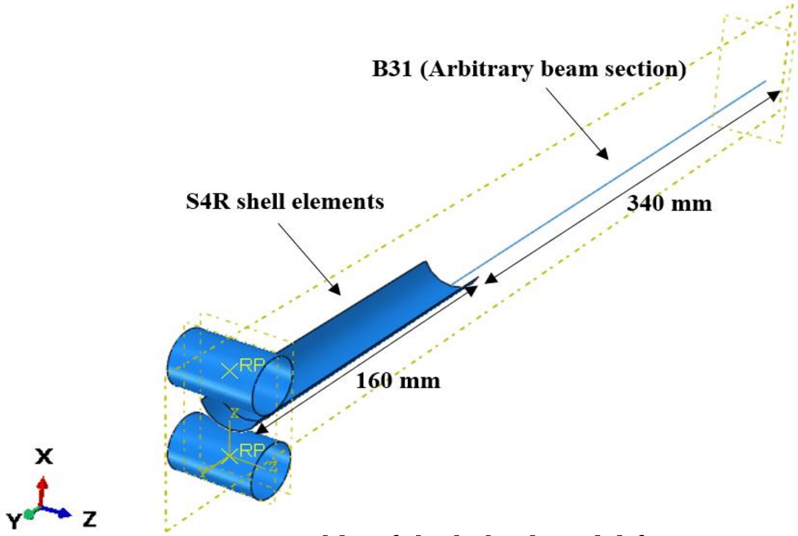

Figure 3.5: Assembly of the hybrid model for stage 01

The length of the tape spring strip which is modelled using shell elements was decided using the results observed discussed in Section 3.3. Similar to the benchmarking model, the front edge of the tape spring modelled using shell elements is attached to the hub enforcing a surface-to-surface contact with a kinetic friction coefficient of 0.18 (Wilson, 2017) and a frictionless general contact everywhere else while excluding the contact surfaces that were already defined in the surface-to-surface contact definition. A penalty contact method is used as the mechanical constraint formulation in both cases.

The B31 beam section should be defined with appropriate curvature compatible with the arc shape of the tape spring. This can be achieved either by defining the correct moment of inertia values (I_{11}, I_{12}, I_{22}, and J) derived from the geometric cross-section or by giving the 1 and 2 coordinates and the thickness for each segment defined by the coordinates of the cross-section so that Abaqus will automatically calculate the moment of inertia from the given input. The former can be done using the generalized beam section and the latter can be achieved using the arbitrary beam section option in the Abaqus 'profile' option in the property menu (see Figure 3.6). An arbitrary beam section profile is used to define the section profile in this model.

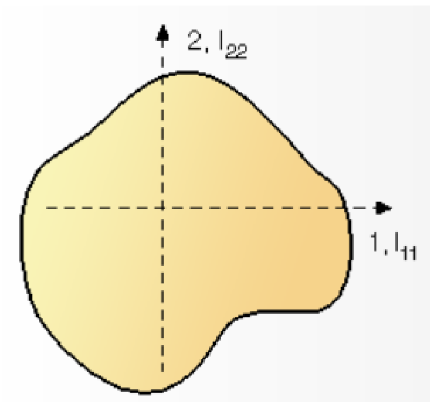

(b) Generalized beam section

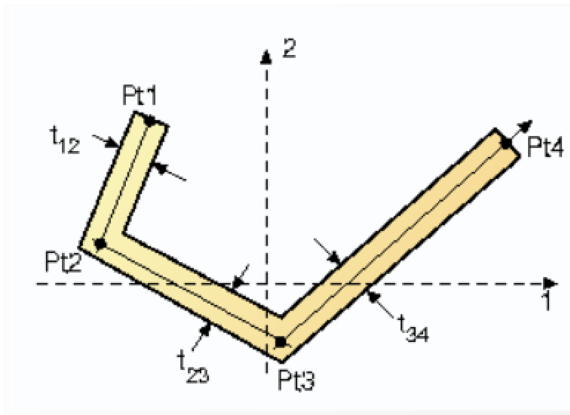

(b) Arbitrary beam section

Figure 3.6: Different methods available in Abaqus to define beam sections

The coordinates of the arbitrary beam section were defined such that the resultant centroid of the curve in the beam cross-section is compatible with the centroid of the cross-section curved tape spring strip modelled using shell elements. A slight distance should be kept between the shell and beam surfaces at the interface to avoid any errors due to overlapping issues. According to the distance defined, the coordinates of the beam section profile should be adjusted to maintain appropriate compatibility between the surfaces and therefore a smooth displacement field.

The crucial point that needs to be tackled in the hybrid model is the force/bending moment transfer between the shell-beam interface. In this sense, the compatibility between the active nodes between the finite elements connected at the interface should be ensured. As far as this model is concerned, this requirement is satisfied as the finite elements S4R and B31 both have 1,2,3,4,5 and 6 nodes activated. As mentioned before, the shell-beam interface should be capable of transferring especially the bending moments which can be achieved by having a beam-like behaviour. Several techniques were explored to achieve this as shown in Figure 3.7.

(a) MPC Beam | (b) Kinematic coupling | (c) Structural distributing coupling

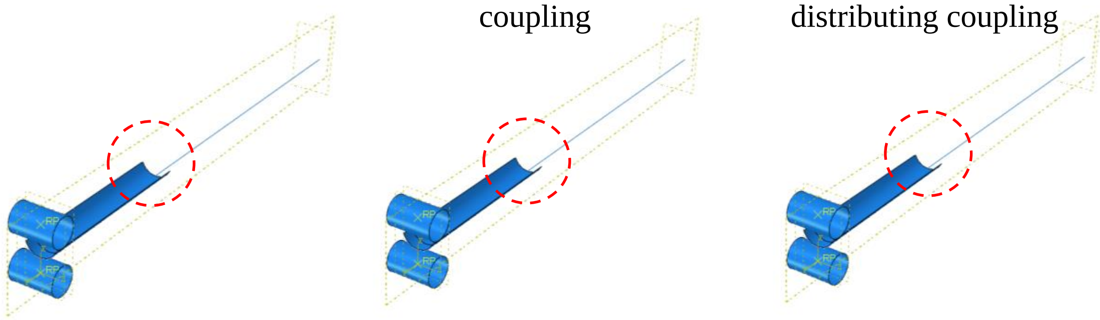

Figure 3.7: Different techniques available to ensure moment transfer between shell-beam interface

For any type of Multi-Point Constraint (MPC), the master node can be either a single node or a set of nodes however, the subsequent (slave) should be a set of nodes. Hence, the front end of the tape spring strip which is modelled using beam sections is taken as the master node whereas the far edge of the tape spring strip which is modelled using shell elements was taken as the slave nodes. As shown in Figure 3.8, The MPC beam type is used to provide a rigid beam between two nodes in order to confine the displacement and rotation at the first node to the displacement and rotation at the second node, which corresponds to the presence of a rigid beam between the two nodes.

The same behaviour can be obtained using coupling constraints. Kinematic coupling binds the motion of the coupling nodes (slave nodes) to the reference node's rigid body motion (master node). Constraining all 3 translational degrees of freedom will demonstrate a rigid body motion where the slave nodes will follow the master node. Constraining all 3 rotational degrees of freedom along with all 3 translational degrees of freedom will exhibit a behaviour equivalent to the MPC beam. The same can be achieved using structural distribution coupling. Similarly, this type of coupling constraints the motion of coupling nodes to that of the reference node. However, in contrast to kinematic coupling, by using weight factors the transmission of loads can be controlled in structural distribution coupling. All 3 translational degrees of freedom are by default constrained in this coupling. To ensure the transfer of bending moments, all 3 rotational degrees of freedom should be constrained manually in this option.

MPC Beam constraint was used in this study to connect the beam-shell interface.

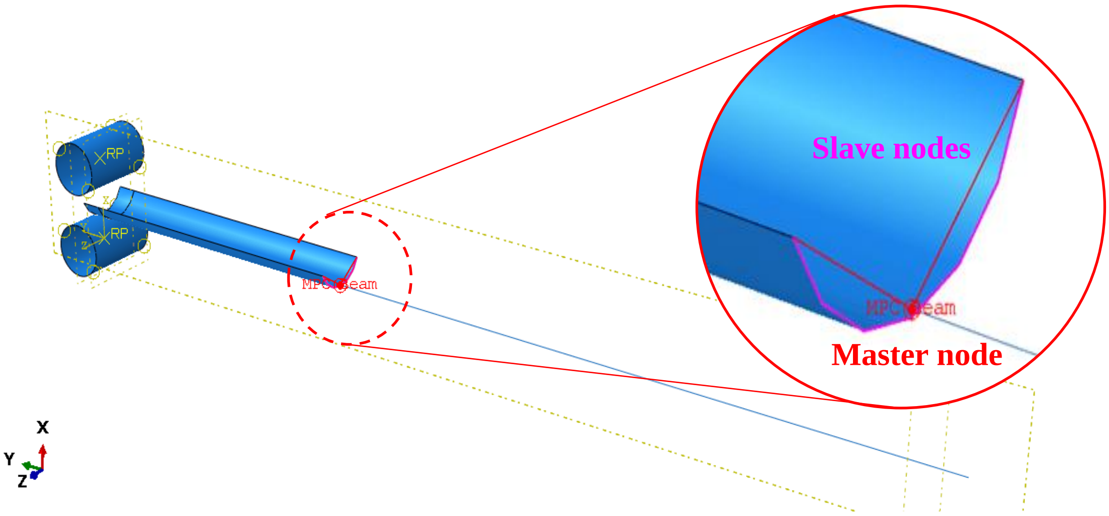

Figure 3.8: MPC beam constraint used at the shell-beam transition

Two steps were defined in this simulation. One being the flattening (1.0 seconds) and the other being the coiling of 1.5 radians (1.0 seconds). The same pull force and viscous pressure were applied similarly to the benchmarking model. Each boundary condition was applied with a smooth step amplitude definition. The boundary conditions activated in the hybrid model are shown in the Table 3.3.

Table 3.3: Loads and boundary conditions activated in stage 01 of the hybrid model

Description	Node set	Flattening 0 -1 (s)	Coiling 1-2 (s)
Hub	Rigid bodies	UR3 = 1.5	UR3 = 1.5
Roller	Rigid bodies	U1 = -15	U3 = -15
General contact applied (Frictionless)	All nodes	✓	✓
Surface to surface contact applied (Friction at the front end)	Front edge surface of the tape spring and external surface of the hub	✓	✓
Apply a pulling/tension force at the free end of the tape spring strip modelled using shell elements	End nodes		CF2 = -1N
Apply viscous pressure on the external faces of the tape spring	Surfaces of the tape spring		p = 5.2e^{-6}

3.5 Flowchart for import analysis

The next important stage in the hybrid model is to import the results from the first stage of the simulation which is discussed in Section 3.4 into the second stage of the simulation. This is referred to as the 'import analysis' in Abaqus. This allows the user to import deformed mesh and its associated material state from a previous simulation as a predefined state into a subsequent simulation. It also provides the freedom to transfer results and model information in between Abaqus/Standard or Abaqus/Explicit analyses, respectively.

This can be achieved by first running the hybrid model discussed in Section 3.4 and once results are obtained, a copy of that same model can be made within the same Abaqus/CAE file. In this newly copied model, changes can be made to create the 2nd stage of the hybrid model. The process of import analysis has been shown in Figure 3.9.

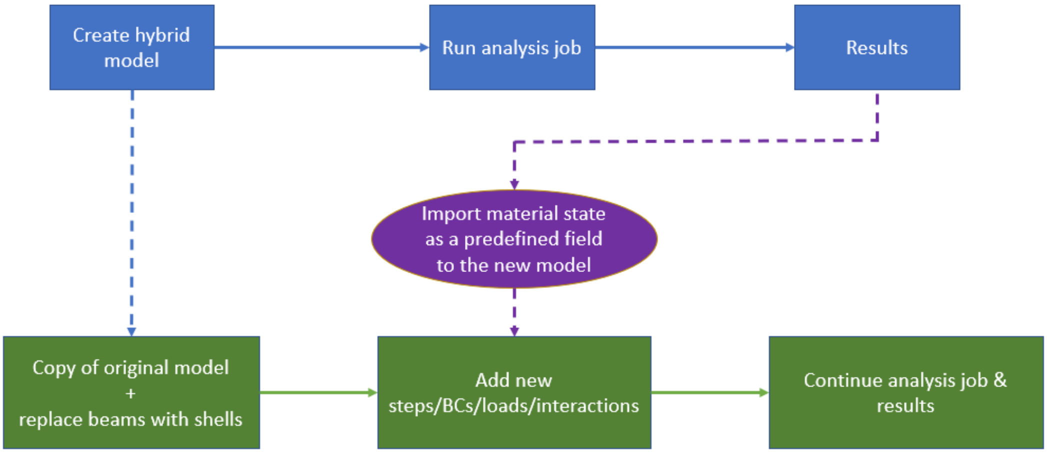

Figure 3.9: Flow chart for the import analysis

Here, a 160 mm of length in the beam section will be replaced with shell elements (see Figure 3.10), and the remaining length will be modelled with beam elements and connected using appropriate constraints as discussed in Section 3.4. As shown in Figure 3.11, the two tape spring strips with shell elements can be connected again using kinematic coupling or structural distribution coupling to exhibit appropriate beam-like behaviour as discussed earlier.

3.6 Beam-Shell hybrid model – Stage 02

The important point to note in the 2nd stage of the model is that during the first stage of the simulation, the tape spring has already been coiled 1.5 radians.

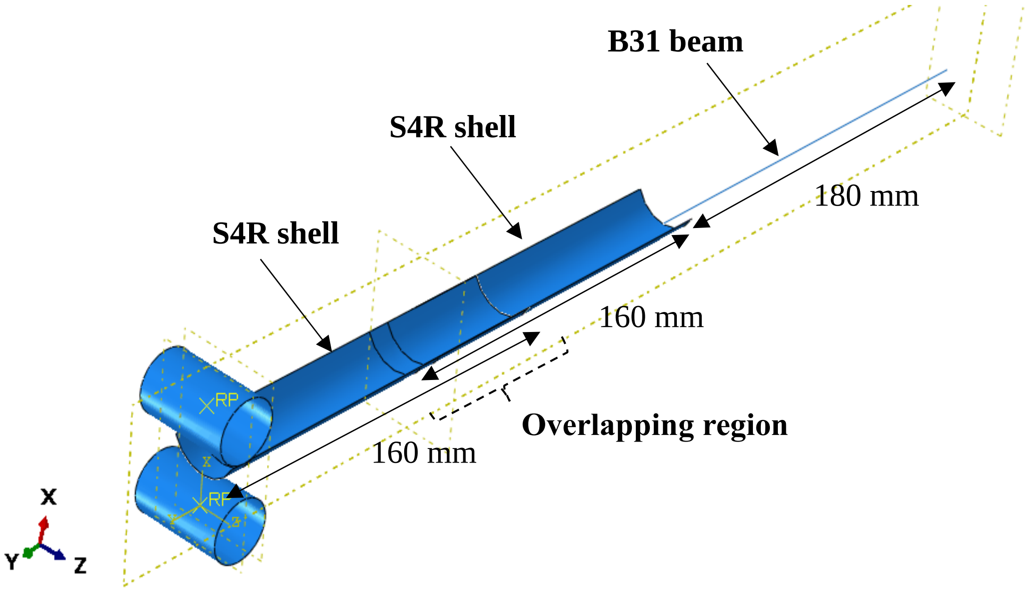

Figure 3.10: Assembly of the hybrid model for stage 02

Hence, when these results are imported to the next stage, the tape spring strip that had been attached to the hub will already be coiled by 1.5 radians which is approximately 20 mm in length. Hence, when attaching the two strips of tape springs modelled using shell elements together, the near edge of the second strip should be overlapped by a length approximately equal or more than equal to the length that has already been coiled with the far edge of the first strip to avoid any gaps in the visualization of the simulation results.

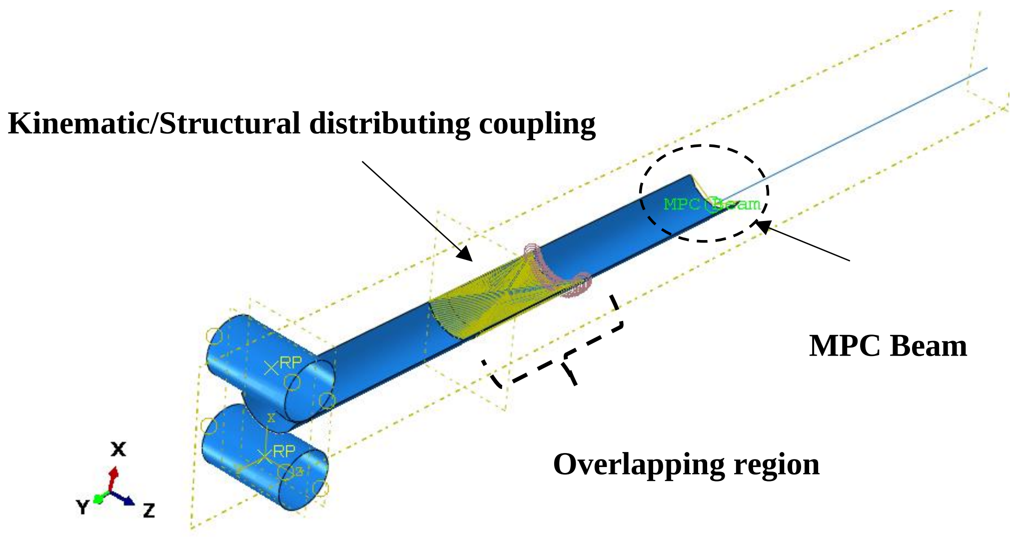

Figure 3.11: Constraint conditions used in the hybrid model – Stage 02

In stage 02, to allow further coiling of the overall tape spring, a new coiling step is defined with a rotation of 1.5 radians (1.0 seconds). The coiling results from stage 01 can be imported as a predefined field to the initial state of the second stage of the model. Similar to the benchmarking model, the front edge of the tape spring modelled using shell elements is attached to the hub enforcing a surface-to-surface contact with a kinetic friction coefficient of 0.18 and a frictionless general contact everywhere else while excluding the contact surfaces that were already defined in the surface-to-surface contact definition. A penalty contact method is used as the mechanical constraint formulation in both cases. The same pull force and viscous pressure are applied similarly to the benchmarking model. When defining the boundary condition for the coiling step, one should keep in mind to continue to define the smooth step amplitude from where it ended in the previous stage of the model. The boundary conditions activated in stage 02 of the hybrid model are shown in Table 3.4.

Table 3.4: Loads and boundary conditions activated in stage 02 of the hybrid model

Description	Node set	Coiling 2-3 seconds
Hub	Rigid bodies	UR3 = 1.5
Roller	Rigid bodies	U1 = -15
Tape spring strip modelled using beam elements	End node	U3 = 0
General contact applied (Frictionless)	All nodes	✓
Surface to surface contact applied (Friction at the front end)	Front edge surface of the tape spring and external surface of the hub	✓
Apply a pulling/tension force at the free end of the tape spring	End nodes of the second tape spring strip modelled using shell elements	CF2 = - 1 N
Apply viscous pressure on the external faces of the tape spring	Surfaces of the tape spring	$p = 5.2e^{-6}$

3.7 Summary of the chapter

This chapter discussed the methodology of preparing the benchmarking model, i.e., the full shell model for coiling and deployment mechanics. The commercially available software Abaqus was used to develop the model. Most material and geometrical parameters were chosen from previous literature so that the numerical results can be verified against them. All loads and boundary conditions activated during each step of the simulation have been tabulated. Contact conditions in this model are of utmost importance and the relevant friction coefficients used here were taken from previous experimental research as explained in Section 3.1. Several challenges have been tackled when developing the benchmarking model such as conducting a quasi-static simulation, ensuring the energy balance in the system, smooth load application, viscous pressure to avoid any excess kinetic energy of vibration effects etc. which are discussed in detail in this chapter.

4. RESULTS

4.1 Theoretical results

Using the theoretical equation proposed in Section 2.2, λ vs. time and therefore the unspooled length vs. time was plotted. It can be observed that the full deployment occurs within 0.44 s. At this stage, no air-drag effects have been considered. At the beginning of coiling the effective coiling radius will be as same as the hub radius which is 12.7 mm. However, as the tape coils multiple times around the hub, the effective coiling radius will increase and reach a final coiling radius. Seffen (1999) has not considered this hence, the calculations have been performed assuming the coiling radius to be constant to the initial coiling radius (= hub radius) throughout (see Figure 4.1). As seen in that graph, the rate of uncoiling gradually reduces meaning that when r is at its maximum, i.e., at the beginning of the deployment, the rate at which the tape spring uncoils is greater than that of the rate when $r \rightarrow r_0$. Hence a greater proportion of the length of the tape spring can be expected to uncoil at the beginning. This is also true for the rate of strain energy release per length (Q) as given in Eq.(2.29). Q will be higher at the beginning compared to the Q when $r \rightarrow r_0$.

4.1.1 Variation of effective coiling radius

The important point to note in Eq.(2.20) is that there are two variables in the same ordinary differential equation (ode) namely, the ‘r’ and ‘λ’. Meaning that both these parameters are functions of time. Neglecting the variation of hub radius with time when solving the ode can be fundamentally erroneous. One could assume that the hub radius will remain unchanged and attempt to solve Eq.(2.20) however, this is not true as the initial radius of coiling (r_{hub}) will keep on increasing to a final coiling radius (r) due to the tape coiling multiple times around the hub until a particular final coiling radius is reached. As an attempt to eliminate the effects from coiling radius in Eq.(2.20) the following modification can be done.

Assume n = number of cycles coiled and h = tape thickness. Then we can develop Eq.(4.1) as follows.

$$n = \frac{r - r_{hub}}{h} \tag{4.1}$$

Length of the tape on the hub (x) = $2 * \pi * n * \left(\frac{r + r_{hub}}{2}\right) = \pi * n * (r + r_{hub})$ (4.2)

Substitute for n in Eq.(4.1) from Eq.(4.2) and we get Eq.(4.3),

$$x = \pi * \left(\frac{r - r_{hub}}{h}\right) * (r + r_{hub}) = \frac{\pi}{h}\left(r^2 - r_{hub}{}^2\right) \tag{4.3}$$

We know $\lambda = \frac{L-x}{L} \rightarrow r^2 = \frac{(1-\lambda)L + \frac{\pi}{h} r_{hub}{}^2}{\frac{\pi}{h}}$, by substituting this in Eq.(2.12) we get Eq.(4.4),

$$\dot{\lambda} = \sqrt{\frac{6\mu R\alpha}{\rho L^4} \left(\frac{(1-\lambda)L + \frac{\pi}{h} r_{hub}{}^2}{\frac{\pi}{h}}\right) \frac{1}{\lambda}} \tag{4.4}$$

This results in a non-linear ordinary differential equation that can be solved using MATLAB ode45 function (see Figure 4.1).

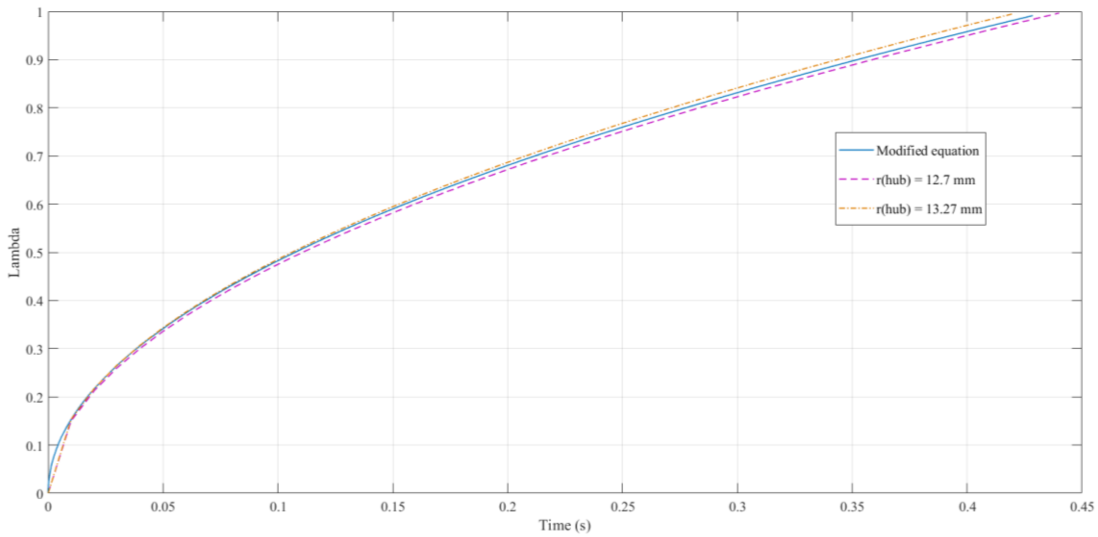

Figure 4.1: λ vs. deployment time when the effective coiling radius is equal to the (a) hub radius (12.7 mm), (b) final coiling radius (13.27 mm) and, (c) effective coiling radius calculated using the modified equation

The results were plotted against Eq.(2.20) when $r = r_{hub} = 12.7$ mm and $r = 13.27$ mm (from Eq.(2.27) for coiling angle of 36 radians). As seen in Figure 4.1, these plots tend to exhibit a linear behaviour initially which is not fundamentally acceptable as Eq.(2.20) is basically in the form of a parabola. In contrast to that, the modified equation projects a smoother curve. Moreover, during the first half of the deployment, the modified equation tends to overlap with the theoretical results when r = 13.27 mm and later projects towards the graph when r_{hub} = 12.7 mm corroborating to the true deployment behaviour. The modified equation results in a deployment time of 0.438 seconds which falls in between 0.42 s (r = 13.27 mm) and 0.44 s (r_{hub} = 12.7 mm). In overall, the modified equation shows better deployment behaviour taking both λ and varying coiling radius into consideration.

The variation of coiling radius can be plotted against time (see Figure 4.2) which further confirms the altering nature of the coiling radius which must be taken into account when capturing the deployment behaviour. The graph shows how the coiling radius varies from 13.27 mm at the beginning of the deployment to 12.7 mm at the end of deployment reaching the natural hub radius.

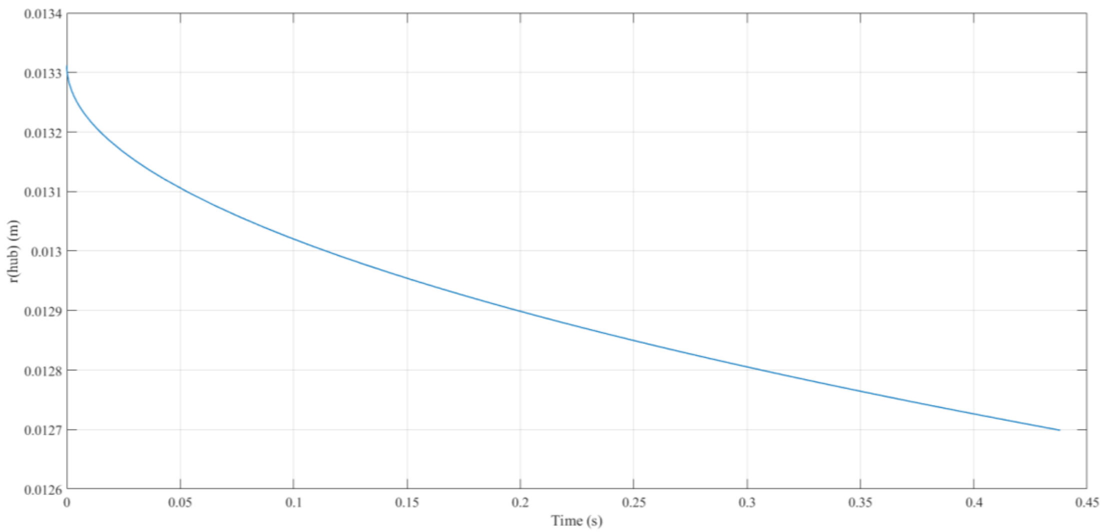

Figure 4.2: Variation of effective hub radius with respect to time

However, in the simulations an initial unspooled length is present, and this has to be accounted for when calculating the deployment time. Using the modified equation this can be conveniently accounted for, by taking whatever the initial unspooled length present as a ratio to the total tape length (λ_0) and substituting that as an initial condition when solving the (modified) non-linear ordinary Eq.(4.4) (see Figure 4.6).

4.1.2 Variation of tension force

As per Figure 2.1, three main regions have been identified with respect to coiling of a tape spring around a hub or a spool. Given that the geometrical parameters in the current study led to a coiling ratio of 0.84, this study was mainly analyzed with a focus of the bending-dominated region. However, Eq.(2.6) and (2.9) lay out the effect of coiling ratio on the tension force applied at one end of the tape spring in the bending-dominated region and tension-dominated region respectively. As opposed to Eq.(2.9) which demonstrates a linear variation between the coiling ration and the tension force, Eq.(2.6) demonstrates a non-linear variation between the said parameters. It is important to note that these results have been derived considering multiple coiling ratio scenarios.

That being said, for a given scenario with a particular coiling ratio, the results obtained in Section 4.1.1 suggests that this tension force applied may also vary due to the effect of variation of the effective hub radius during coiling and deployment. When the said effect is incorporated, Eq.(4.5) and (4.6) can be obtained that suggest for a given case of R and L, the tension force is not constant but rather varies in a non-linear manner in both the bending-dominated region and the tension-dominated region with respect to λ, i.e. during coiling and deployment.

Bending-dominated region:

$$T = \frac{D\alpha}{2R}\left(\frac{R^2}{\frac{(1-\lambda)L + \frac{\pi}{h}{r_{hub}}^2}{\frac{\pi}{h}}} - 1\right) \tag{4.5}$$

Tension-dominated region:

$$T = \frac{48D\left(1-\cos\frac{\alpha}{2}\right)}{\alpha^3 R}\ \frac{\sqrt{\left(\frac{(1-\lambda)L + \frac{\pi}{h}{r_{hub}}^2}{\frac{\pi}{h}}\right)}}{R} \tag{4.6}$$

Figures 4.3 and 4.4 show the aforementioned non-linear variation between λ and T, however, since $0 < \lambda < 1$, this non-linearity is not significantly visible hence, can be deemed as almost linear. In this study where R=15.1 mm and L=500 mm, in Figure 4.3 it can be observed that 0.38 N > T > 0.27 N for full deployment. Similarly, T varies in both bending-dominated and especially in tension-dominated regions where localized folds tend to form.

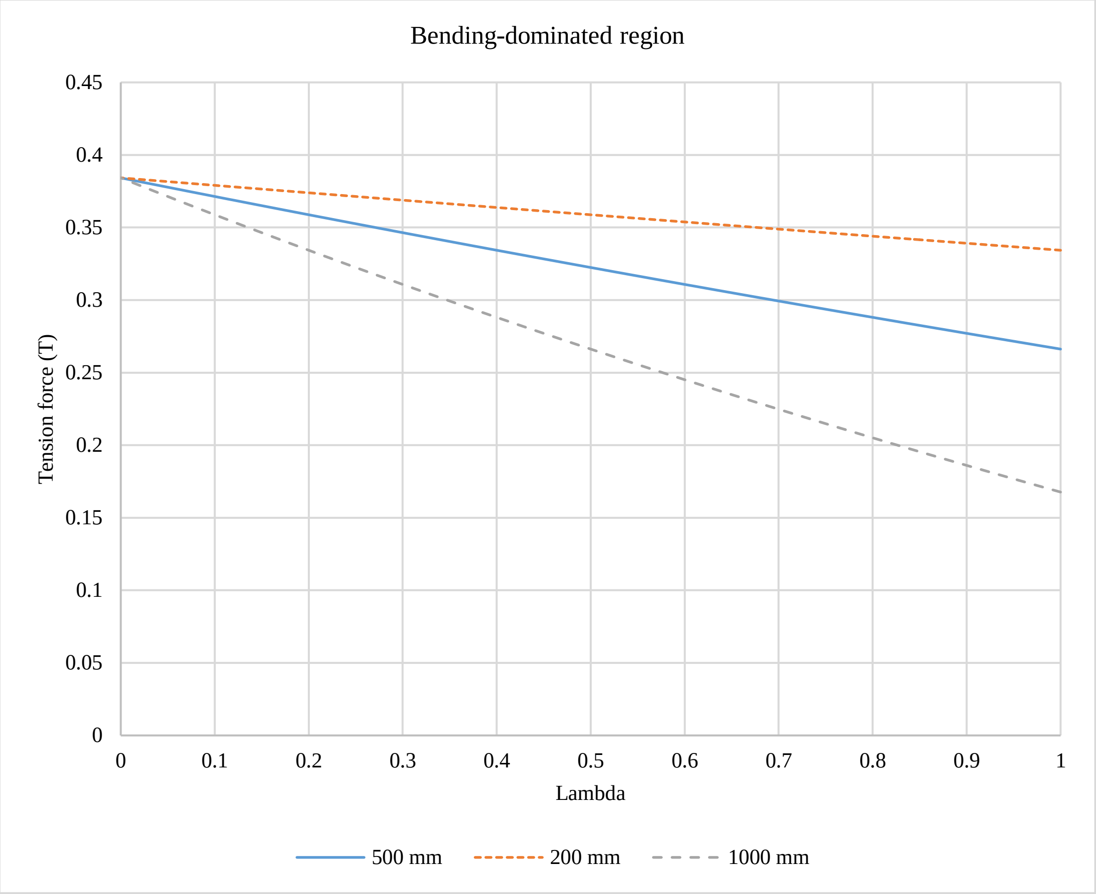

Figure 4.3: λ vs. tension force in the bending dominated-region

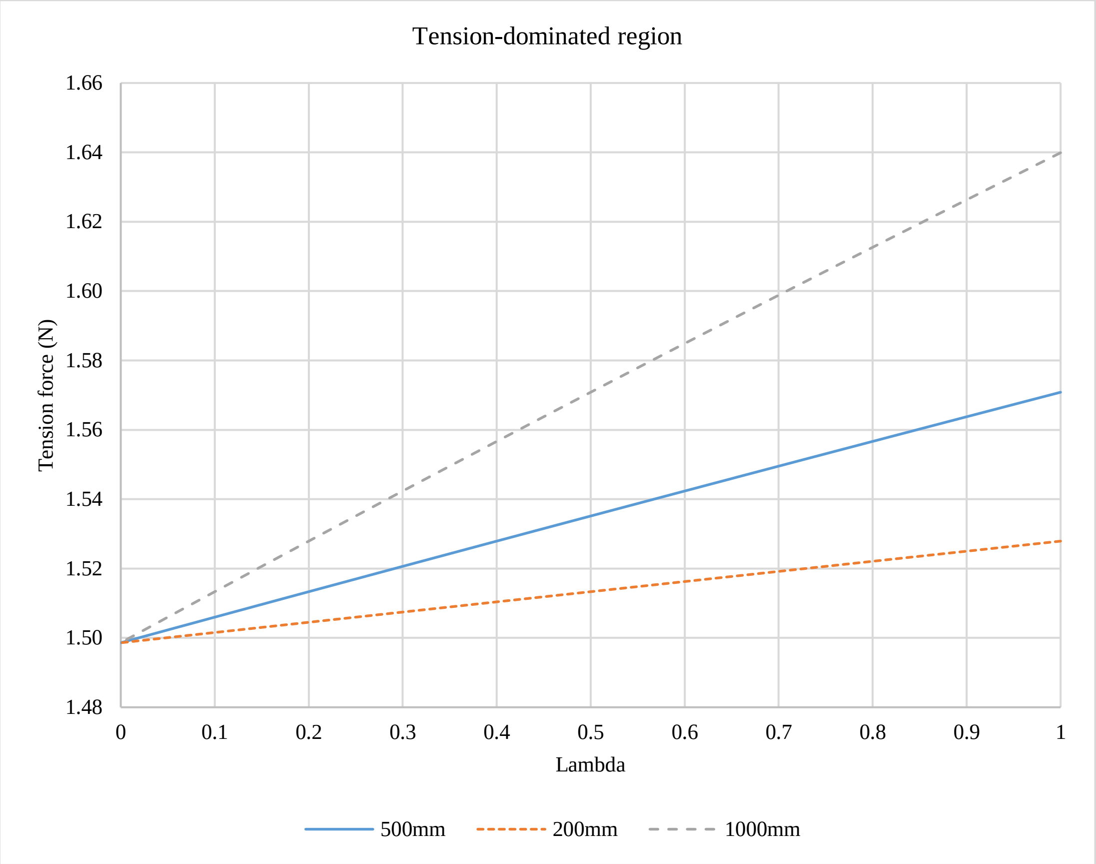

Figure 4.4: λ vs. tension force in the tension dominated-region

In addition to that, for longer tape springs the variation of the tension force required significantly increase. Hence, in real scale satellites and space structures which incorporate tape springs of meters of lengths, this result will be prominent. Since there is only limited power available in such systems in space for coiling and deployment control, accurate prediction of required tension force is of critical use. However, extensive future work remains on the validation of results obtained in this section in terms of experiments and other numerical methods available albeit, one can use this as a good starting point.

4.2 Numerical results (benchmarking model)

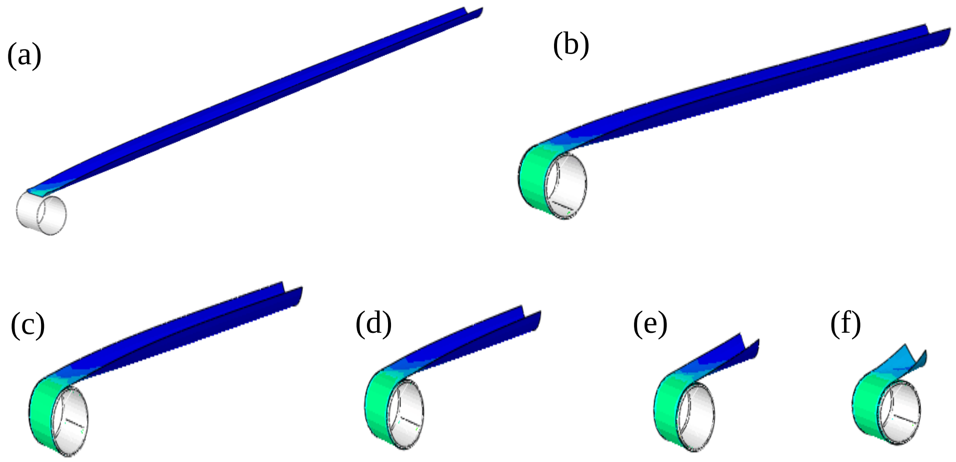

Figure 4.5: Coiling of tape-spring during the time steps, t = (a) 2 s, (b) 7 s, (c) 10 s, (d)14 s, (e) 17 s, and (f) 20 s

Different configurations of coiling behaviour during several time steps have been captured as shown in Figure 4.5. At the beginning, the coiling radius is equal to the hub radius (Figure 4.5(a)) but after multiple coils, the effective coiling radius increases and reaches a final coiling radius (Figure 4.5(f)). The uncoiling /deployment of the tape spring obtained from the Abaqus simulation is shown in Figure 4.6.

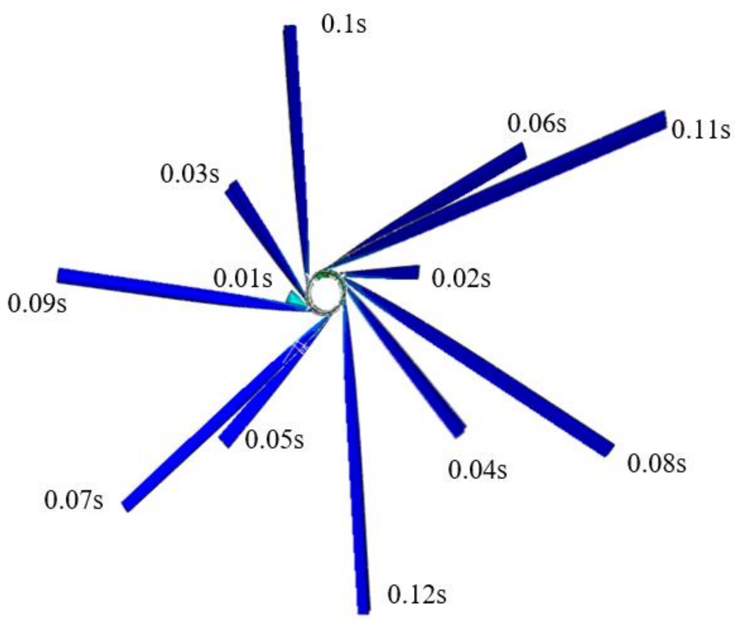

Figure 4.6: Deployment of tape-spring during the first 0.12 seconds

Within 0.43 s the full deployment was reached in the FE simulation as opposed to the theoretical deployment time obtained which was 0.44 s (assuming $r=r_{hub}=12.7$ mm and without considering the initial unspooled length) (see Figure 4.7).

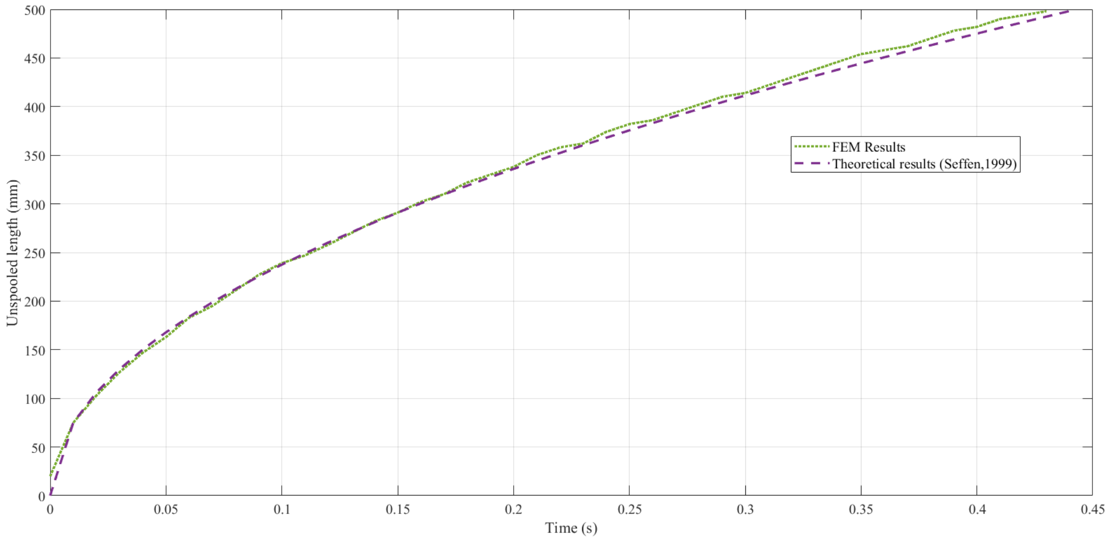

Figure 4.7: Variation of unspooled length with respect to deployment time obtained for FE simulation and the theoretical equation (Seffen, 1999)

4.2.1 Effect of varying coiling radius

However, in order to eliminate the effects from the varying coiling radius, numerical results were plotted against the modified equation. The modified theoretical equation suggests a deployment time of 0.438 s which best collates with FE results (see Figure 4.8). As mentioned in Seffen's work, "For a more detailed comparison, because it is difficult to take accurate measurements right at the end of the deployment, it is best to compare the time taken to reach 90% deployment, i.e. = 0.9, in these tests" (Seffen,1999). Hence, a better comparison between the theoretical and numerical deployment time can be made by considering the deployment time for 90% of the deployed length as this would eliminate the effect from end effects. Considering 450 mm of length which is 90% of the total length gives a deployment time of approximately 0.35 seconds for both theoretical numerical results for the deployment time.

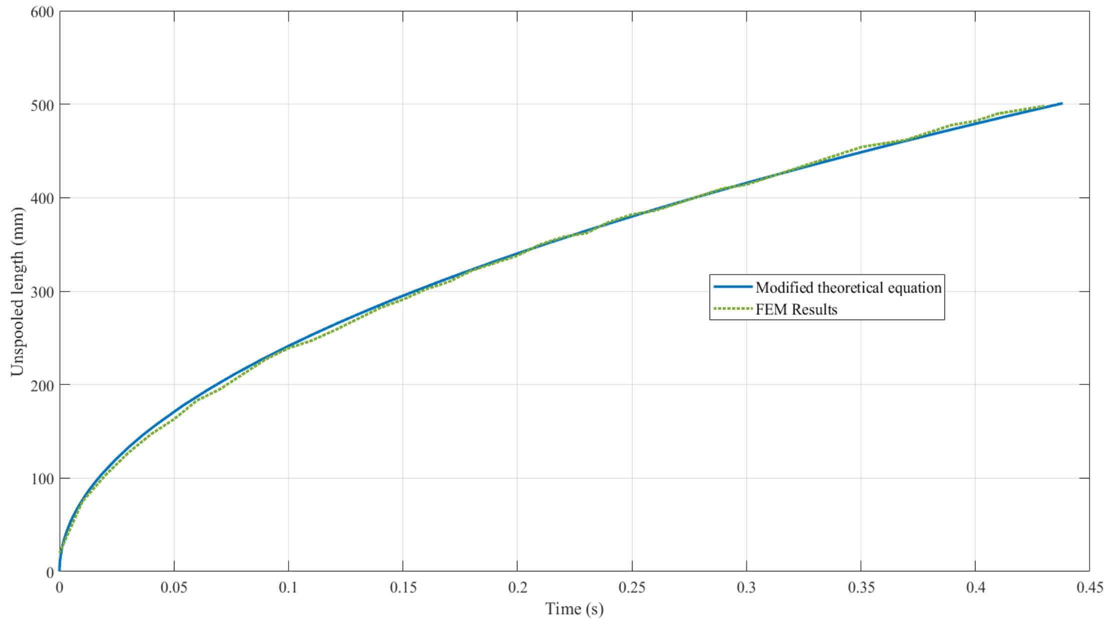

Figure 4.8: Variation of unspooled length with respect to deployment time obtained for FE simulation and the modified equation

4.2.2 Effects from initial unspooled length

With the aim of eliminating the effects from the initial unspooled length and to further check the behaviour, FEM results were plotted against the modified equation for both initial unspooled length and varying coiling radius using Eq.(4.4) (see Figure 4.9). As mentioned earlier, this can be conveniently achieved by assigning an initial condition for λ (=20mm/500mm=0.04) that corroborates to the initial unspooled length of 20 mm. Evidently, the modified equation presents better deployment behaviour.

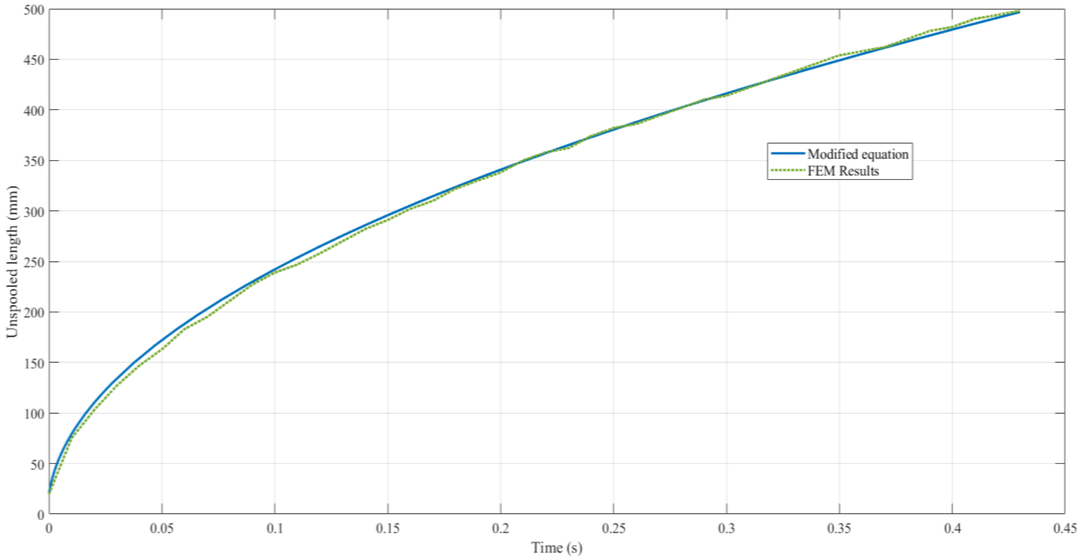

Figure 4.9: Variation of unspooled length with respect to deployment time when an initial unspooled length is present for modified equation and FE results

However, for a single tape, the effects from varying coiling radius and initial unspooled length may seem insignificant but in real satellite or space structures with multiple tape springs or booms which are in meters of length, a significant variation in coiling radius will occur, therefore in deployment time. Hence, the proposed modified Eq.(4.4) will be quite useful to emphasize such effects and deviations in this sense.

4.3 Variation of curvature

4.3.1 Transverse curvature

As explained in Section 2.1.3, the longitudinal and transverse curvature for the deformed configuration can be calculated as follows when $R = 15.1\,mm$ and $r_c = 12.7\,mm$ as shown in Eq.(4.7) and Eq.(4.8).

$$K^0 = \begin{pmatrix} K^0_{xx} \\ K^0_{yy} \\ K^0_{xy} \end{pmatrix} = \begin{pmatrix} \frac{-1}{R} \\ 0 \\ 0 \end{pmatrix} = \begin{pmatrix} -0.066\,mm^{-1} \\ 0 \\ 0 \end{pmatrix} \tag{4.7}$$

$$K^1 = \begin{pmatrix} K^1_{xx} \\ K^1_{yy} \\ K^1_{xy} \end{pmatrix} = \begin{pmatrix} 0 \\ \frac{1}{r_c} \\ 0 \end{pmatrix} = \begin{pmatrix} 0 \\ 0.0787\,mm^{-1} \\ 0 \end{pmatrix} \tag{4.8}$$

The corresponding variation and plot of transverse curvature vs. non-dimensional transverse coordinate (z measured in the transversal direction) obtained from Abaqus are as shown in Figures 4.10 and 4.11.

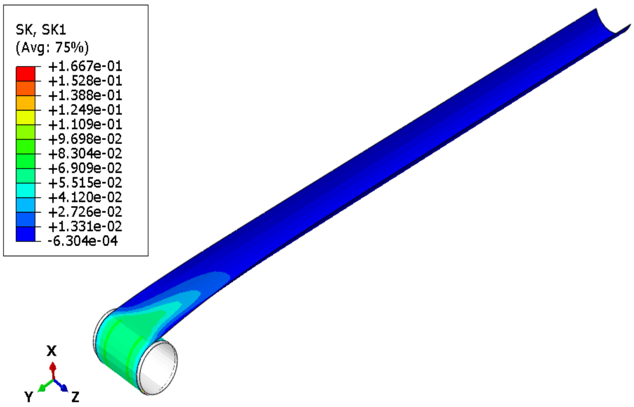

Figure 4.10: Variation of transverse curvature obtained from Abaqus

The flattened region of the tape spring subtends around the hub resulting in a curvature that of the hub itself. This has been reflected in the plot of transverse curvature of the flattened region with a curvature of $\frac{1}{r_c}$ within the edges of the tape spring. However, about 40% of the central region of the width still maintain the original curvature of $\frac{1}{R}$ as shown in Figure 4.11.

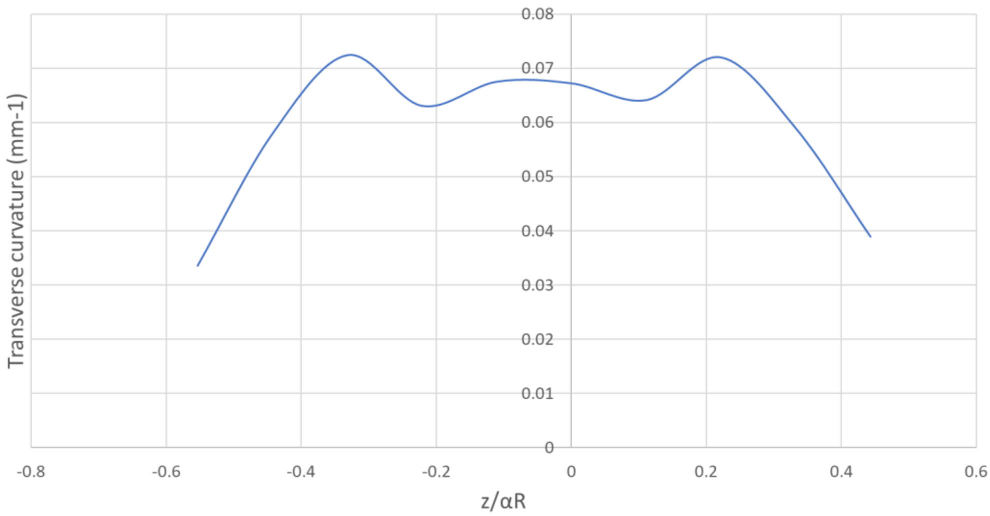

Figure 4.11: Transverse curvature vs. non-dimensional transverse coordinate (z measured in the transversal direction)

4.3.2 Longitudinal curvature

The corresponding variation and plot of longitudinal curvature vs. true distance measured along the centreline of the tape spring in the longitudinal direction has been obtained from Abaqus are as shown in Figures 4.12 and 4.13.

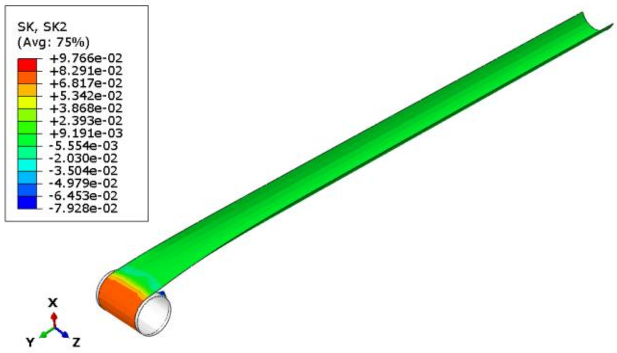

Figure 4.12: Variation of longitudinal curvature obtained from Abaqus

As shown in Figure 4.13, the plot shows that the region coiled around the hub exhibits a curvature $\frac{1}{r_c}$ which is similar to that of the hub itself. The region attached to the hub with a no-slip friction condition shows a non-smooth change in curvature which could be due to the contact/attachment. A sudden negative curvature can be observed followed by a gradual reduction of longitudinal curvature in the transition region. However, this converges to zero in the undeformed region.

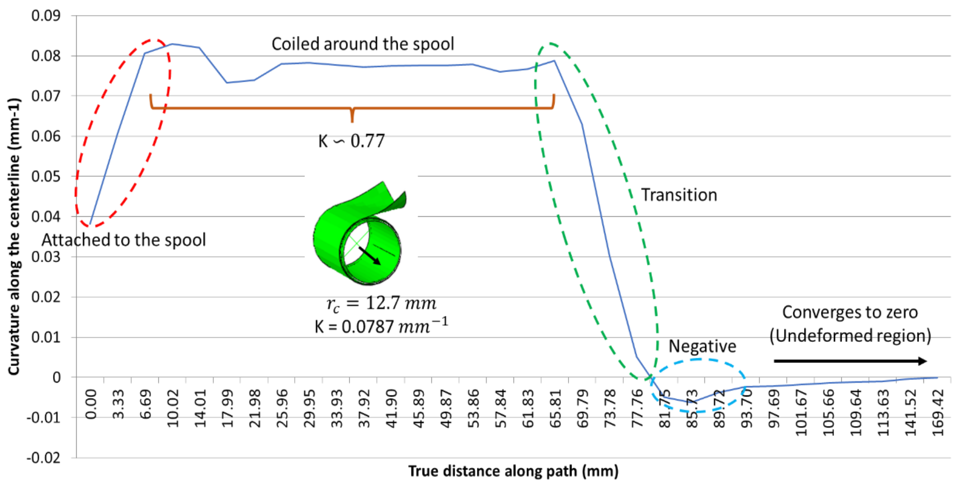

Figure 4.13: Longitudinal curvature vs. true distance measured along the centerline of the tape spring in the longitudinal direction

4.4 Stress distribution

As explained in Section 2.1.4, the transverse (σ_{11}) and longitudinal stresses (σ_{22}) (see Figure 4.14) can be calculated as given in Eq.(4.7) and Eq.(4.8).

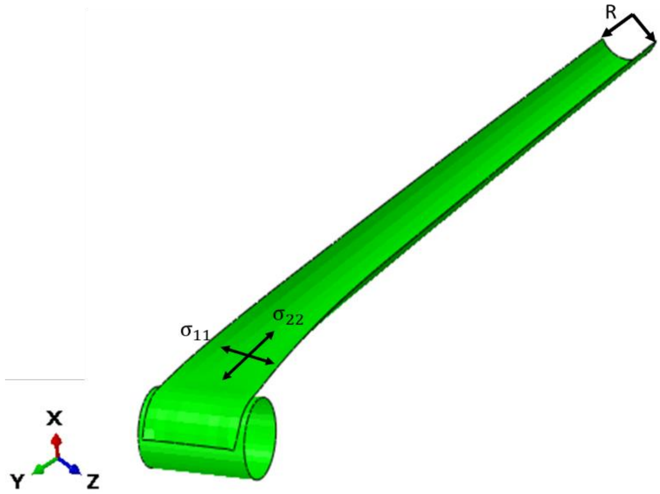

Figure 4.14: Transverse (σ_{11}) and Longitudinal stress (σ_{22}) directions of the tape spring

Using Eq.(4.7) and Eq.(4.8) the change in respective curvatures can be calculated as shown in Eq.(4.9) and Eq.(4.10);

$$\Delta K_x = K_{xx}^1 - K_{xx}^0 = \frac{-1}{R} \tag{4.9}$$

$$\Delta K_y = K_{yy}^1 - K_{yy}^0 = \frac{1}{r_c} \tag{4.10}$$

This assumes a perfect flattening in the cross-section although it is not the case in reality because there will be affects due to edge conditions. However, as long as the inner region is considered this theory will be fairly valid.

From $Kirchoff - Love\ plate\ theory$, the strain distribution can be derived as shown in Eq.(4.11) and Eq.(4.12);

$$\varepsilon_{xx} = \varepsilon_{xx}^0 + z\Delta K_{xx} = -\frac{z}{R} \tag{4.11}$$

$$\varepsilon_{yy} = \varepsilon_{yy}^0 + z\Delta K_{yy} = \frac{z}{r_c} \tag{4.12}$$

With that the plane stress for thin plates/shells can be derived as shown in Eq.(4.13);

$$\begin{pmatrix}\sigma_{11}\\ \sigma_{22}\end{pmatrix} = \frac{E}{1-\nu^2}\begin{bmatrix}1 & \nu\\ \nu & 1\end{bmatrix}\begin{bmatrix}\varepsilon_{xx}\\ \varepsilon_{yy}\end{bmatrix} = \frac{E}{1-\nu^2}\begin{bmatrix}-\frac{z}{R}+\nu\frac{z}{r_c}\\ -\nu\frac{z}{R}+\frac{z}{r_c}\end{bmatrix} \tag{4.13}$$

By considering the number of cycles of coiling, z can be determined. By substituting $z = 0.1$ mm considering 2 full cycles of coiling in this case, the stresses σ_{11} and σ_{22} can be obtained for the top and bottom surfaces of the tape spring.

4.4.1 Transverse stress distribution

As shown in the Figure 4.15 the transverse stress (σ_{11}) of the bottom surface along the cross-section obtained from the numerical model vs. non-dimensional transverse coordinate (z measured in the transversal direction) was plotted and was compared against the predicted transverse stress from the plate theory above. For about 70% of the inner region of the width, the numerical stress value well agrees with the predicted theoretical value. However, the stress distribution is not so smooth at the edges of the tape spring due to edge effects.

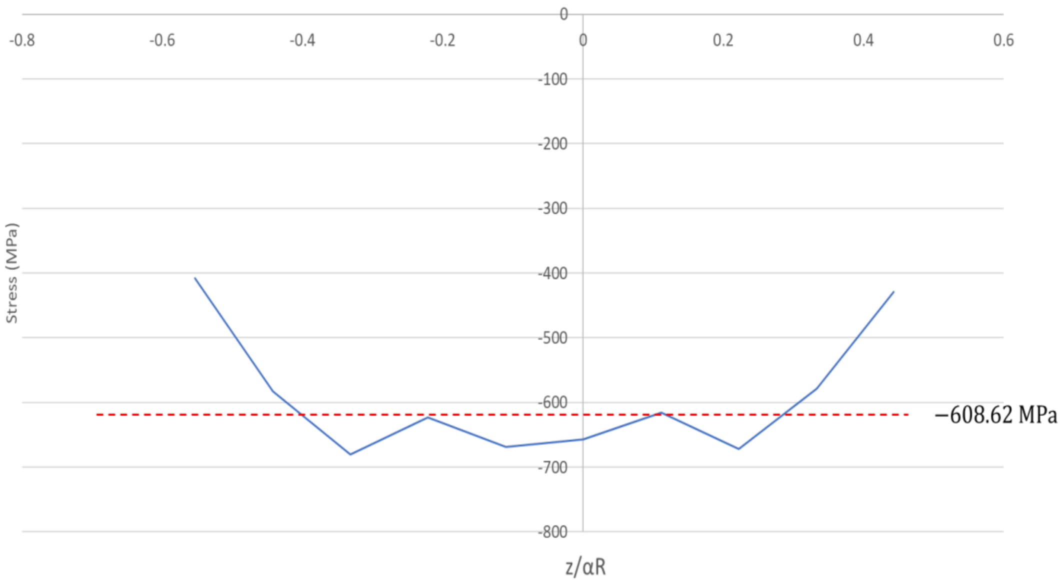

Figure 4.15: Transverse stress (σ_{11}) of the bottom surface along the cross-section obtained from the numerical model vs. non-dimensional transverse coordinate (z measured in the transversal direction)

4.4.2 Longitudinal stress distribution

Figure 4.16 shows the longitudinal stress (σ_{22}) of the bottom surface obtained from the numerical model vs. non-dimensional transverse coordinate (z measured in the transversal direction) was plotted along the cross-section of the tape spring and was compared against the predicted transverse stress from the plate theory as in Eq.(4.13).

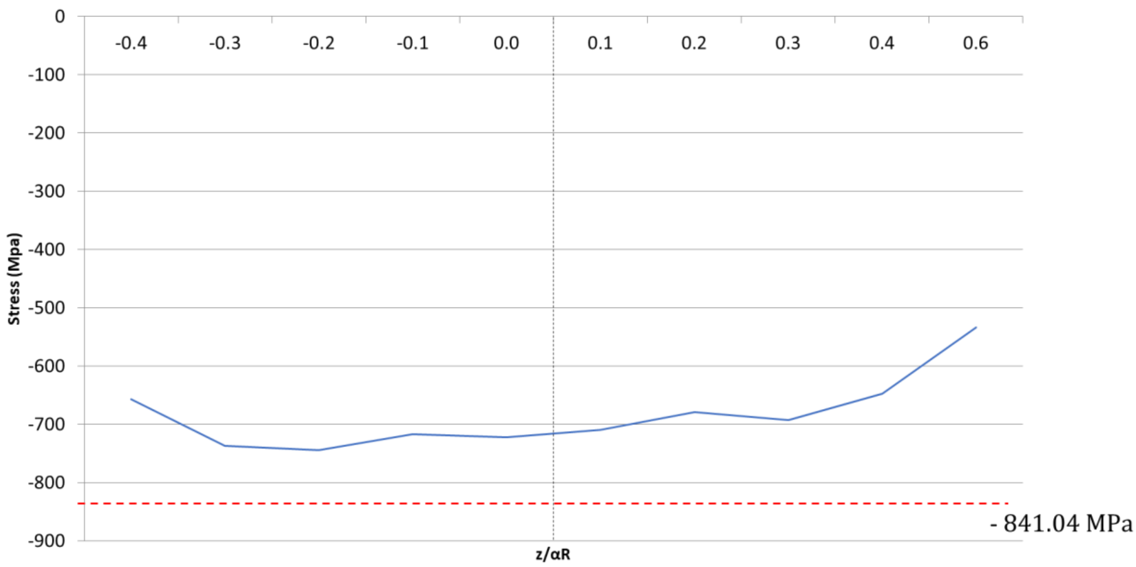

Figure 4.16: Transverse stress (σ_{22}) of the bottom surface obtained from the numerical model vs. non-dimensional transverse coordinate (z measured in the transversal direction)

For about 60% of the inner region of the width the numerical model predicts the longitudinal stress along the cross-section predicted by the plate theory with an error margin of about 17%. As seen in Figure 4.15 and 4.16 the stresses seem to be symmetric in the inner region ensuring that the tape spring has been subjected to pure bending with no stretching as formulated by the analytical study explained in Section 2.1.4. However, the results don’t agree well towards the edges as predicted although ideally the free edges should have a stress of σ_{22} = 0.

As shown in the Figure 4.17 the longitudinal stress (σ_{22}) of the bottom surface obtained from the numerical model vs. true length along the centreline in the longitudinal direction was plotted and was compared against the predicted longitudinal stress from the plate theory above.

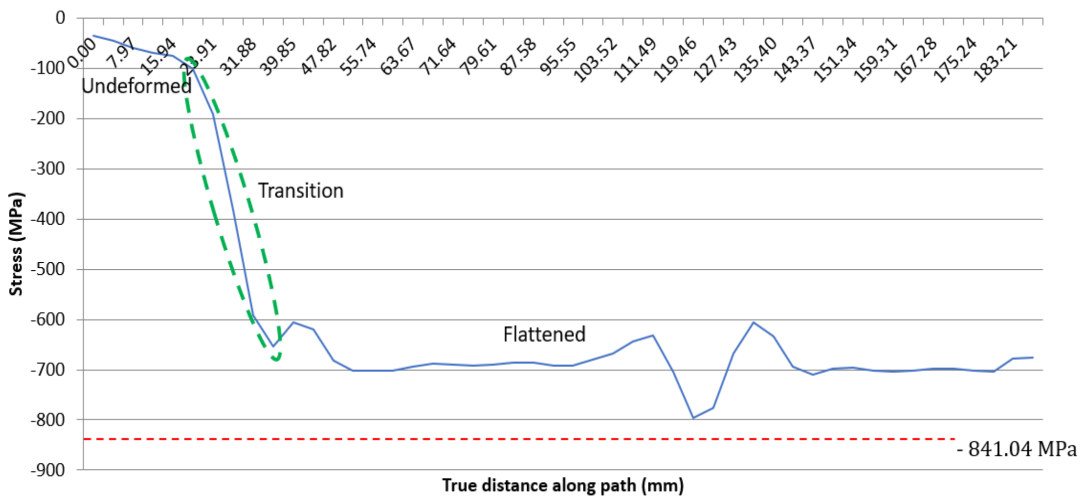

Figure 4.17: Longitudinal stress (σ_{22}) of the bottom surface obtained from the numerical model vs. true length along the centerline in the longitudinal direction

As seen in the Figure 4.17, stress in the undeformed region tends to zero however, there is a gradual increase of longitudinal stress in the transition region and it continues to exist in the flattened region. The numerical model predicts the longitudinal stress along the true longitudinal length predicted by the plate theory with an error margin of about 17%.

4.5 Energy variation of the model

The energy variation of the simulation is of utmost importance as the tape spring is flattened and coiled under quasi-static conditions and allowed to dynamically deploy there onwards. As seen in Figure 4.18, during the flattening, coiling, and stowage steps the kinetic energy of the system is 1% of the internal energy ensuring it to be negligible throughout as expected. This ensures that no dynamic excitations have occurred in the system.

Since, Abaqus provides the global kinetic energy of the system, the kinetic energy of the rigid bodies in the system has been deducted. Moreover, the bending strain energy gained by the tape spring is about 1.3 J. This can be further corroborated by theoretically calculating the stored strain energy using U=μR^2αϴ=1.33 J.

Hence, in terms of stored strain energy, the model provides satisfactory results. Some energy spikes can be seen in strain energy at the beginning which is during the flattening step as no viscous damping was enabled at this step unlike in coiling and stowage steps. However, the total energy of the system is zero which deems the energy balance of the system as satisfactory.

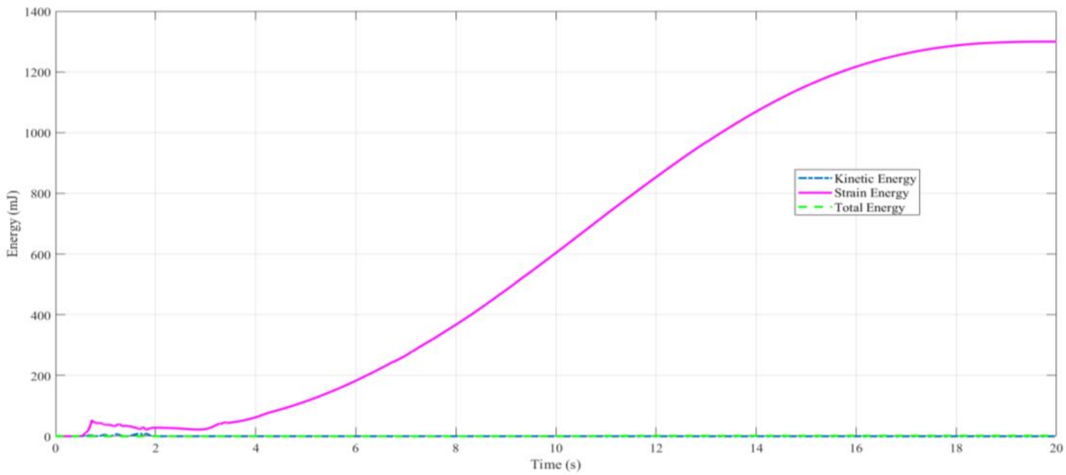

Figure 4.18: Variation of Kinetic energy Strain energy and Total energy (energy balance) in the explicit simulation

Since the developed model produces satisfactory results, this can be used in developing the reduced-order beam-shell model as discussed in the next section. Further, this model will be quite useful when exploring the coiling mechanics of setups with $\frac{r_c}{R}$ >1 which is still under research.

4.6 Numerical results (Beam-shell hybrid model)

Smooth transitions of the displacement and stress fields were obtained during the first stage of the hybrid model as seen in Figure 4.19.

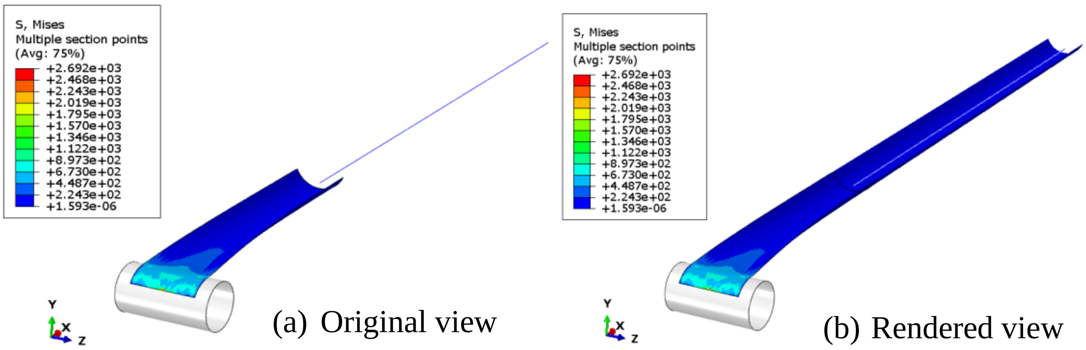

(a) Original view (b) Rendered view

Figure 4.19: Resultant coiling simulation of the hybrid model – Stage 01

After performing the import analysis with parallel to the first stage of the model, the second stage of the hybrid model was performed.

Smooth transitions of the displacement and stress fields were obtained during the second stage of the hybrid model as seen in Figure 4.20.

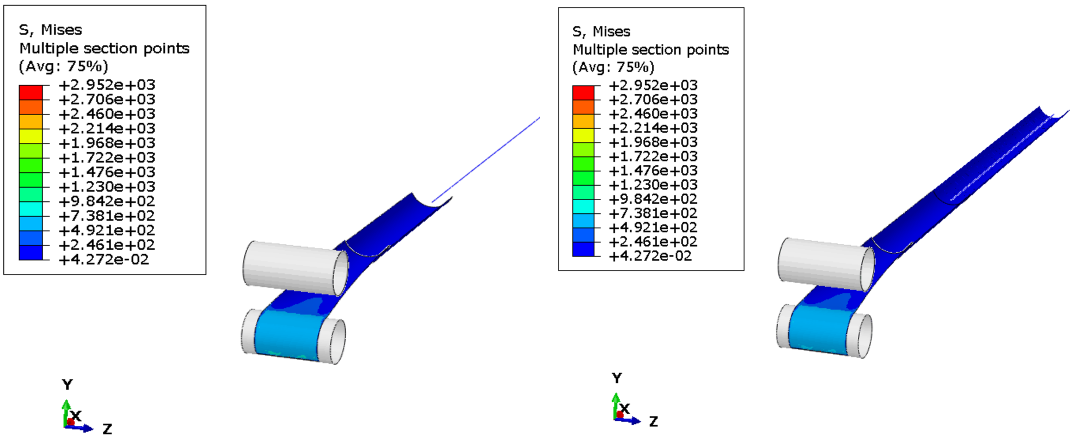

(a) Original view (b) Rendered view

Figure 4.20: Resultant coiling simulation of the hybrid model – Stage 02

4.7 Computational time of the analyses

As discussed in Section 3.1, it is generally recommended to keep the minimum element edge length of the mesh ≤ 1% of tape spring length in the transverse direction as shown by preliminary convergence studies for a sufficient level of accuracy (Seffen et.al, 2019). Hence, in the reduced order model where only a portion of the length is modelled using shell elements, it was observed that the mesh size is governed by the length of the portion of the tape spring that is modelled using shell elements in order to obtain an accurate behaviour of coiling. This obviously results in a mesh size that is smaller than that of the benchmarking model (1 mm ≤ 1% of tape spring length of 160 mm = 1.6 mm) hence, comparatively a larger number of degrees of freedom to be handled. A series of convergence tests were performed to confirm this statement.

The complete coiling of the tape was not performed in the reduced order model hence, a direct comparison against the benchmarking model is not acceptable. However, the information on the computational time tabulated in Table 4.1 gives a reasonable background to commence and reflect on the computational efficiency in each simulation condition explored in this study.

Table 4.1: Summary of information on computational efficiency of the analyses

Description	Benchmarking model	Hybrid-Stage 01	Hybrid-Stage 02
Mesh size (mm)	4	1	1
Coiling angle	36	1.5	1.5
Step time (s)	20	2	1
Total CPU time (hours)	5:32:16	15:42:28	14:57:23
Stable time increment	6.69E-07	1.52E-07	1.52E-07
Total number of variables in the model (Degrees of freedom plus max no. of any Lagrange multiplier variables)	17,712	63,636	99,378

Evidently, a significant reduction in the stable time increment can be observed in the reduced order model. This is mainly due to the reduced mesh size in the shell elements used. Moreover, as discussed in Section 3.2, in Abaqus/Explicit, the stable time increment is calculated per element hence, a single element with the smallest stable time increment can dominate and decide the simulation time of the entire model. With the use of constraint such as MPC, tie, coupling or connectors in Abaqus/Explicit alone can reduce the computational speed, i.e., a longer computational time. This is further reflected in the details given in Table 4.2 with respect to the beam-shell hybrid model.

Table 4.2: Comparison of stable time increments in the beam-shell hybrid model

Part instance	Tape spring (Shell)	Tape spring (Beam)
No. of elements	5760	34
Average stable time increment	1.89E-07	2.37E-06
Smallest stable time increment	1.89E-07	2.37E-06

As mentioned earlier, the stable time increment in the model is governed by the shell elements. Hence, it is crucial to approximate a compromise between the computational time and the stable time increment when developing the beam-shell hybrid model.

Evidently, Abaqus/Explicit cannot be recommended when developing the hybrid model. Abaqus/Standard may be a better option as it is ideal for many quasi-static dynamic problems with relatively low speeds. Accurate stress solutions can be obtained using Abaqus/Standard for such problems and comparatively faster simulations can be expected as the stable time increment does not depend on the smallest mesh size of the model. That being said, the beam-shell hybrid model comes with number of complex contact conditions as well as coupling constraints which will have to be tackled strategically when adopting Abaqus/Standard. An alternative that can be recommended is to perform a mesh sensitivity analysis which is independent to that of the preliminary convergence studies adopted in Section 3.1 for this study. A detailed mesh sensitivity analysis can be performed for the benchmarking model as well as the beam-shell hybrid model and evaluate the impact of mesh size on the overall computational time of the respective simulations.

When working with real scale space structures consisting of very long narrow thin shells, this beam-shell hybrid modelling technique developed will provide significant potential in modelling coiling and deployment behaviour of long narrow self-deployable structures.

4.8 Summary of the Chapter

This chapter mainly describes the results of the analytical and numerical studies carried out. Existing theoretical framework is further improved to incorporate effects from the varying hub radius. This gave better deployment behavior and therefore more accurate deployment time. Finite element simulations were first performed for the benchmarking model and the results were validated against the theoretical results both existing and modified. Variation of energy was also checked as a way of validating the numerical model. Before moving to the reduced order model, i.e., the beam-shell hybrid model, an approximation for the ploy region length was derived from a previous study and the numerical results obtained from the benchmarking model. The hybrid model was developed preliminary under two stages. In real space industrial applications where the tape springs are in meters of lengths, this beam-shell hybrid modelling technique will be quite useful when performing numerical simulations.

5. CONCLUSIONS AND RECOMMENDATION

Recent advances in space exploration call for smaller space structures that can be reconfigured to achieve large surfaces when in operation. Compact, lightweight structures that can be folded or coiled up for launch have been made possible thanks to self-deployable booms. These can then be self-deployed in orbit to support a variety of small spacecraft systems. However, prior understanding of deployment behaviour is important before launch. This thesis has conferred a detailed study on reduced order model techniques in predicting the deployment behaviour of coiled long-narrow thin shells known as tape springs.

Coiling, stowage, and deployment stages demonstrate considerable cross-section deformation of the tape-spring. The ploy region that is in between the flattened and undeformed region is critical as the gain/release of the strain energy, i.e., the strain energy gradient during coiling and deployment is maintained through this region. Developing full shell numerical models in this sense will require extensive hardware and software resources. With the aim of reducing the computational time and effort, reduced order model techniques can be explored.

The developed numerical benchmarking model well agrees with the theoretical framework that has previously been established in terms of deployment time and stored strain energy. However, the previous theoretical study has not considered the effects of varying hub radius as well as any initial unspooled length prior to deployment. Incorporation of such effects and further improvements to the theoretical equations suggest better deployment behaviour. Several energy checks were also performed to validate the developed benchmarking model. ‘S’ curve of the strain energy gain ensures smooth loading application. This has further been validated by the theoretical results obtained for the strain energy. Zero kinetic energy throughout the simulation suggests a quasi-static simulation without any unnecessary spurious energy generations. The total energy of the system is zero which deems the energy balance of the system as satisfactory.

The proposed numerical benchmarking model gives results that satisfactorily collate with the theoretical results in terms of the stored strain energy during coiling and deployment time. Within the confidence level of the theoretical framework, the FEM simulation can be deemed valid in predicting the coiling and deployment mechanics of thin shells.

Out of the available numerical techniques to reduce computational time and effort, use of 1D finite elements for the undeformed region and 2D finite elements for the flattened and ploy regions to develop hybrid (reduced order) models is explored. The proposed reduced order model technique is based on the benchmarking model developed and validated earlier. A stage-wise development is followed when incorporating shell elements into the benchmarking model, especially taking the critical regions into consideration. The study conducted on approximating the length of the ploy region provides an interesting observation for the arc length used in the theoretical equation. For bending of tape springs, it has been suggested to use the arc length of the tape spring. However, it was observed that in the benchmarking model, ploy length is most compatible when the projected arc length is used in the equation. Confirmation on these needs more studies albeit this has been adopted in the reduced order model when approximating the length of the shell region that should be modeled using shell elements.

At this stage, a detailed analysis on the computational efficiency of the proposed model is not possible as it depends on many factors. Especially, the effect of mesh size on the accuracy of results should be explored by conducting a sensitivity analysis for the reduced order model. For models with finer mesh sizes and many constraints and complex contact conditions the stable time increment should be handled carefully because very small stability limits will lead to large number of increments and will increase the simulation time drastically as opposed to what is expected in a reduced order model. Use of Abaqus/Standard or performing a mesh sensitivity analysis prior to choosing the mesh size of the model without relying on the preliminary convergence studies that was adopted from a previous study can be recommended in tackling the excessive computational time in the beam-shell hybrid model that was developed in this study. However, in relating to real scale satellite and space structure systems where the tape springs/booms are used in meters of lengths, the deduced reduced order technique will enable the reduction of the computational time and effort required in modelling such systems when compared to full shell models.

6. REFERENCES

Belytschko, T., Liu, W. K., Moran, B., and Elkhodary, K. Nonlinear finite elements for continua and structures. John Wiley & sons, 2013.

Brinkmeyer, A., Pellegrino, S., & Weaver, P. M. (2016). Effects of Long-Term Stowage on the Deployment of Bistable Tape Springs. *Journal of Applied Mechanics*, *83*(1), Art. No. 011008.

Calladine, C. R. (1988). *The Theory of Thin Shell Structures 1888–1988*. https://doi.org/10.1243/PIME_PROC_1988_202_020_02

Gonçalves, R., Ritto-Corrêa, M., & Camotim, D. (2010). A large displacement and finite rotation thin-walled beam formulation including cross-section deformation. *Computer Methods in Applied Mechanics and Engineering*, *199*, 1627–1643. https://doi.org/10.1016/j.cma.2010.01.006

Guinot, F., Bourgeois, S., Cochelin, B., & Blanchard, L. (2012). A planar rod model with flexible thin-walled cross-sections. Application to the folding of tape springs. *International Journal of Solids and Structures*, *49*(1), 73–86. https://doi.org/10.1016/j.ijsolstr.2011.09.011

Hoffait, S., Brüls, O., Granville, D., Cugnon, F., & Kerschen, G. (2010). Dynamic analysis of the self-locking phenomenon in tape-spring hinges. *Acta Astronautica*, *66*(7), 1125–1132. https://doi.org/10.1016/j.actaastro.2009.10.001

Mallikarachchi, H. M. Y. C. (2011). *Thin-walled composite deployable booms with tape-spring hinges* [Thesis, University of Cambridge]. https://doi.org/10.17863/CAM.14004

Mallikarachchi, H. M. Y. C., & Pellegrino, S. (2012). Quasi-Static Folding and Deployment of Ultrathin Composite Tape-Spring Hinges. *Journal of Spacecraft and Rockets*. https://doi.org/10.2514/1.47321

Mallol, P., & Tibert, G. (2013). Deployment Modeling and Experimental Testing of a Bi-stable Composite Boom for Small Satellites. In *54th AIAA/ASME/ASCE/AHS/ASC Structures, Structural Dynamics, and Materials Conference*. American Institute of Aeronautics and Astronautics. https://doi.org/10.2514/6.2013-1672

Pedivellano, A., & Pellegrino, S. (2019). Stability Analysis of Coiled Tape Springs. In *AIAA Scitech 2019 Forum*. American Institute of Aeronautics and Astronautics. https://doi.org/10.2514/6.2019-1523

Peterson, L., & Mobrem, M. (2018). Structural Analysis Methodology for Space Deployable Structures using a High-Performance Parallel Nonlinear Finite Element Solver. In *4th AIAA Spacecraft Structures Conference*. American Institute of Aeronautics and Astronautics. https://doi.org/10.2514/6.2017-0852

Pimenta, P., & Campello, E. M. B. (2003). A fully nonlinear multi-parameter rod model incorporating general cross-section in-plane changes and out-of-plane warping. *Latin American Journal of Solids and Structures, 1*, 119–140.

Sadowski, A. J. (2019). On the advantages of hybrid beam-shell structural finite element models for the efficient analysis of metal wind turbine support towers. *Finite Elements in Analysis and Design*, *162*, 19–33. https://doi.org/10.1016/j.finel.2019.05.002

Seffen, K. A., & Pellegrino, S. (1999). Deployment dynamics of tape springs. *Proceedings of the Royal Society of London. Series A: Mathematical, Physical and Engineering Sciences*, *455*(1983), 1003–1048. https://doi.org/10.1098/rspa.1999.0347

Seffen, K. A., Wang, B., & Guest, S. D. (2019). Folded orthotropic tape-springs. *Journal of the Mechanics and Physics of Solids*, *123*, 138–148.

Seffen, K. A., You, Z., & Pellegrino, S. (2000). Folding and deployment of curved tape springs. *International Journal of Mechanical Sciences*, *42*(10), 2055–2073. https://doi.org/10.1016/S0020-7403(99)00056-9

Soykasap, Ö. (2007). Analysis of tape spring hinges. *International Journal of Mechanical Sciences*, *49*(7), 853–860. https://doi.org/10.1016/j.ijmecsci.2006.11.013

S, S., Umakanthan, S., & V, K. (2011). Beam and shell element model for advanced analysis of steel structural members. *Journal of Constructional Steel Research*, *67*, 1789. https://doi.org/10.1016/j.jcsr.2011.05.003

Wilson, L., Gdoutos, E. E., & Pellegrino, S. (2020). Tension-Stabilized Coiling of Isotropic Tape Springs. *International Journal of Solids and Structures*, *188–189*, 103–117. https://doi.org/10.1016/j.ijsolstr.2019.09.010

Wilson, L. L. (2017). *Analysis of Packaging and Deployment of Ultralight Space Structures* [Phd, California Institute of Technology]. https://doi.org/10.7907/Z9B27S96

Živković, M., Kojic, M., Slavković, R., & Grujović, N. (2001). A general beam finite element with deformable cross-section. *Computer Methods in Applied Mechanics and Engineering*, *190*(20–21), 2651–2680. https://doi.org/10.1016/S0045-7825(00)00259-0